Comput Geosci (2014) 18:57–75
DOI 10.1007/s10596-013-9382-y

ORIGINAL PAPER

Coupling multipoint flux mixed finite element methods with continuous Galerkin methods for poroelasticity

Mary Wheeler · Guangri Xue · Ivan Yotov

Received: 12 September 2012 / Accepted: 22 October 2013 / Published online: 16 November 2013

Abstract We study the numerical approximation on irregular domains with general grids of the system of poroelasticity, which describes fluid flow in deformable porous media. The flow equation is discretized by a multipoint flux mixed finite element method and the displacements are approximated by a continuous Galerkin finite element method. First-order convergence in space and time is established in appropriate norms for the pressure, velocity, and displacement. Numerical results are presented that illustrate the behavior of the method.

Keywords Poroelasticity · Geomechanics · Multipoint flux mixed finite element · Continuous Galerkin · Finite volume method

1 Introduction

Fluid motion through porous media and solid deformation are inherently coupled. Applications in the geosciences where such coupling is important include environmental cleanup, petroleum production, solid waste disposal, and carbon sequestration, with field phenomena such as surface subsidence, uplift displacement, pore collapse, cavity generation, hydraulic fracturing, thermal fracturing, wellbore collapse, sand production, and fault activation.

The mathematical model for the coupled fluid-solid system used in this paper is the classical Biot consolidation system in poroelasticity [6, 42] under a quasi-static assumption. The system consists of an equilibrium equation for the solid and a mass balance equation for the fluid. The fluid pressure contributes to the total stress of the solid, and the divergence of the solid displacement represents an additional term in the fluid content. There is a large body of literature on the numerical modeling of the coupled system. In [30–32], Taylor-Hood finite elements are employed for a displacement–pressure variational formulation. A least squares formulation that approximates directly the solid stress and the fluid velocity is studied in [25, 26]. Finite difference schemes on staggered grids designed to avoid nonphysical oscillations at early times have been developed in 1D in [15, 19]. The method in [15] can handle discontinuous coefficients through harmonic averaging. A formulation based on mixed finite element (MFE) methods for flow and continuous Galerkin (CG) for elasticity has been proposed in [36, 37]. The advantage of this approach is that the fluid approximation is locally mass conservative and the fluid velocity is computed directly. Further work addresses the problem of eliminating locking or removal of nonphysical pressure oscillations via the use of discontinuous Galerkin (DG) for elasticity [27, 28, 38]. In [20], a parallel domain decomposition method has been developed for coupling a time-dependent poroelastic model in a localized region with an elastic model in adjacent regions. Each model is discretized independently on nonmatching grids and the systems are coupled using DG jumps and mortars.

M. Wheeler
Institute for Computational Engineering and Sciences,
The University of Texas at Austin,
Austin, TX 78712, USA
e-mail: mfw@ices.utexas.edu

G. Xue (✉)
Shell Technology Center Houston,
Shell International Exploration and Production Co.,
Houston, TX 77082, USA
e-mail: Guangri.Xue@shell.com

I. Yotov
Department of Mathematics, University of Pittsburgh,
Pittsburgh, PA 15260, USA
e-mail: yotov@math.pitt.edu

Applications of the Biot system to the computational modeling of coupled reservoir flow and geomechanics can be found in [11, 17, 18, 41].

The focus of this paper is to develop a discretization method for the poroelasticity system that is suitable for irregular and rough grids and discontinuous full tensor permeabilities that are often encountered in modeling subsurface flows. To this end, we develop a formulation that couples multipoint flux mixed finite element (MFMFE) methods for flow with CG for elasticity. The MFMFE method was developed for Darcy flow in [21, 44, 47]. It is locally conservative with continuous fluxes and can be viewed within a variational framework as a mixed finite element method with special approximating spaces and quadrature rules. The MFMFE method allows for an accurate and efficient treatment of irregular geometries and heterogeneities such as faults, layers, and pinchouts that require highly distorted grids and discontinuous coefficients. The resulting discretizations are cell-centered with convergent pressures and velocities on general hexahedral and simplicial grids. The reader is referred to [45] for the performance of the MFMFE method for flow on a benchmark test using rough 3D grids and anisotropic coefficients.

The MFMFE method was motivated by the multipoint flux approximation (MPFA) methods [2, 3, 13, 14]. In the MPFA finite volume framework, sub-edge (sub-face) fluxes are introduced, which allows for local flux elimination around grid vertices and reduction to a cell-centered pressure scheme. Similar elimination is achieved in the MFMFE variational framework, by employing appropriate finite element spaces and special quadrature rules. The MFMFE method is based on the BDM_1 [9] or the BDDF_1 [8] spaces with a trapezoidal quadrature rule applied on the reference element, [21, 44, 47]. We refer to [23, 24] for a related work on quadrilateral grids using a broken Raviart-Thomas space and to [1, 22] for papers utilizing both approaches.

The choice of CG for elasticity is reasonable if the permeability is not very small and locking is not an issue. As mentioned above, there has been previous work on employing DG for poroelasticity discretizations to eliminate locking [27, 28, 38]. In [28], it was shown that DG degrees of freedom may only be needed in localized regions, while the less expensive CG may be used in the rest of the domain. Since our goal in this paper is to emphasize the applicability of the MFMFE method for flow in the Biot system, we have chosen to consider only CG for elasticity, thus avoiding the more complicated DG notation. Nevertheless, coupling MFMFE for flow with DG or a combination of CG and DG for elasticity is a possible choice that will be studied in future papers.

In this paper, we develop convergence analysis for the MFMFE-CG numerical approximation of the time-dependent poroelasticity system. We study two versions of the method: with a symmetric quadrature rule on simplicial and smooth quadrilateral and hexahedral grids and a nonsymmetric quadrature rule on rough quadrilateral and hexahedral grids. The framework allows for handling hexahedral grids with nonplanar faces defined via trilinear mappings from the reference cube. The backward Euler method is employed for time discretization. Theoretical and numerical results demonstrate first-order convergence in time and space for the fluid pressure and velocity, as well as for the solid displacement.

The rest of the paper is organized as follows. The problem formulation and the numerical approximation are presented in Section 2. Known convergence results for the MFMFE method on pure Darcy flow problem are given in Section 3. The convergence analysis for the continuous in time and the fully discrete schemes is developed in Sections 4 and 5, respectively. Section 6 is devoted to computational experiments. Finally, conclusions are given in Section 7.

2 Problem formulation and discretizations

We first introduce some notations. For a domain $\Omega \subset \mathbb{R}^d$, $d = 2, 3$, let $\|\cdot\|_{k,\infty}$, $k \in \mathbb{R}$, denote the norm in the Sobolev space $W^{k,\infty}(\Omega)$. Let $\|\cdot\|_k$ and $|\cdot|_k$ be the norm and seminorm, respectively, in the Hilbert space $H^k(\Omega)$. The norm in $L^2(\Omega)$ is denoted by $\|\cdot\|$. The $L^2(\Omega)$-inner product is denoted by $(\cdot,\cdot)$ and for $G \subset \partial\Omega$, $\langle\cdot,\cdot\rangle_G$ denotes the $L^2(G)$-inner product or duality pairing. For a tensor-valued function M, let $\|M\|_\alpha = \max_{i,j} \|M_{ij}\|_\alpha$ for any norm $\|\cdot\|_\alpha$.

Let $X \lesssim (\gtrsim) Y$ denote that there exists a positive constant C, independent of the mesh size h and the time step size Δt, such that $X \leq (\geq) CY$. The notation $X \eqsim Y$ means that both $X \lesssim Y$ and $X \gtrsim Y$ hold.

Let $\Omega \subset \mathbb{R}^d$ be a domain with a Lipschitz continuous boundary $\partial\Omega$ and unit outward normal $\mathbf{n}$. The poroelasticity system [6, 42] in Ω over a time interval $(0, T]$, $T > 0$, reads

$$-\nabla\cdot\boldsymbol{\sigma} = \mathbf{f}, \qquad \text{in } \Omega \times (0, T], \tag{2.1}$$

$$\mathbf{z} = -\mathbf{K}\nabla p, \qquad \text{in } \Omega \times (0, T], \tag{2.2}$$

$$\frac{\partial}{\partial t}(c_0 p + \alpha\nabla\cdot\mathbf{u}) + \nabla\cdot\mathbf{z} = s, \qquad \text{in } \Omega \times (0, T], \tag{2.3}$$

where $\mathbf{f}$ is an external force, s is a source or sink term, and

$$\boldsymbol{\sigma} = \lambda\,\mathrm{tr}(\boldsymbol{\epsilon})\,\mathbf{I} + 2\mu\boldsymbol{\epsilon} - \alpha p\,\mathbf{I}, \quad \boldsymbol{\epsilon}(\mathbf{u}) = \frac{1}{2}(\nabla\mathbf{u} + \nabla\mathbf{u}^T). \tag{2.4}$$

In the above constitute equations, $\mathbf{u}(\mathbf{x}, t)$ is the displacement of the porous rock, $p(\mathbf{x}, t)$ is the fluid pressure, $\mathbf{z}(\mathbf{x}, t)$ is the Darcy velocity, $\mathbf{K}(\mathbf{x})$ is a symmetric and uniformly positive definite tensor representing the rock permeability divided by the fluid viscosity, $\boldsymbol{\sigma}(\mathbf{x}, t)$ is the total stress tensor, $c_0 > 0$

is the storage coefficient, α is the Biot–Willis constant, and λ and μ are the Lamé constants

$$\lambda = \frac{E\nu}{(1+\nu)(1-2\nu)}, \quad \mu = \frac{E}{2(1+\nu)}, \tag{2.5}$$

where E is the Young's module and ν is the Poisson's ratio. The gravity force is ignored for simplicity. We assume that there exist constants $0 < k_0 \le k_1$ such that for all $\mathbf{x} \in \Omega$, $\mathbf{K}(\mathbf{x})$ satisfies

$$k_0 \boldsymbol{\xi}^T \boldsymbol{\xi} \le \boldsymbol{\xi}^T \mathbf{K}(\mathbf{x}) \boldsymbol{\xi} \le k_1 \boldsymbol{\xi}^T \boldsymbol{\xi}, \quad \forall\, \boldsymbol{\xi} \in \mathbb{R}^d. \tag{2.6}$$

The above system is supplemented by the following boundary and initial conditions, wherein $\partial\Omega = \Gamma_u \cup \Gamma_\sigma$ and $\partial\Omega = \Gamma_p \cup \Gamma_z$,:

$$\mathbf{u} = 0, \qquad \text{on } \Gamma_u \times (0,T], \tag{2.7}$$
$$\boldsymbol{\sigma}\mathbf{n} = \mathbf{t}_N, \qquad \text{on } \Gamma_\sigma \times (0,T], \tag{2.8}$$
$$p = 0, \qquad \text{on } \Gamma_p \times (0,T], \tag{2.9}$$
$$\mathbf{z}\cdot\mathbf{n} = 0, \qquad \text{on } \Gamma_z \times (0,T], \tag{2.10}$$
$$p(\cdot,0) = p_0, \qquad \text{in } \Omega, \tag{2.11}$$
$$\mathbf{u}(\cdot,0) = \mathbf{u}_0, \qquad \text{in } \Omega. \tag{2.12}$$

We assume that $s(\cdot,t) \in L^2(\Omega)$, $\mathbf{f}(\cdot,t) \in (L^2(\Omega))^d$, $\mathbf{u}_0 \in (L^2(\Omega))^d$, and $p_0 \in L^2(\Omega)$. The no-flow and homogeneous Dirichlet boundary conditions are considered for simplicity.

The following functional spaces will be used in the weak formulation.

$$\mathbf{V} = \left\{\mathbf{v} \in (H^1(\Omega))^d : \mathbf{v} = 0 \text{ on } \Gamma_u\right\},$$
$$\mathbf{Z} = \{\mathbf{z} \in H(\mathrm{div};\Omega) : \mathbf{z}\cdot\mathbf{n} = 0 \text{ on } \Gamma_z\},$$
$$W = L^2(\Omega).$$

The weak formulation is: find $\mathbf{u}(\cdot,t) \in \mathbf{V}$, $\mathbf{z}(\cdot,t) \in \mathbf{Z}$, and $p(\cdot,t) \in W$, $t \in [0,T]$, such that

$$a(\mathbf{u},\mathbf{v}) - \alpha(p, \nabla\cdot\mathbf{v}) = (\mathbf{f},\mathbf{v}) + \langle \mathbf{t}_N, \mathbf{v}\rangle_{\Gamma_\sigma}, \quad \forall\, \mathbf{v} \in \mathbf{V}, \tag{2.13}$$
$$(\mathbf{K}^{-1}\mathbf{z},\mathbf{q}) - (p, \nabla\cdot\mathbf{q}) = 0, \quad \forall \mathbf{q} \in \mathbf{Z}, \tag{2.14}$$
$$\left(\frac{\partial}{\partial t}(c_0 p + \alpha\nabla\cdot\mathbf{u}), w\right) + (\nabla\cdot\mathbf{z}, w) = (s,w), \forall\, w \in W, \tag{2.15}$$
$$\mathbf{u}(\cdot,0) = \mathbf{u}_0, \quad p(\cdot,0) = p_0, \tag{2.16}$$

where

$$a(\mathbf{u},\mathbf{v}) = (\boldsymbol{\sigma}(\mathbf{u}) : \boldsymbol{\epsilon}(\mathbf{v})) = (2\mu\boldsymbol{\epsilon}(\mathbf{u}) : \boldsymbol{\epsilon}(\mathbf{v})) + (\lambda\nabla\cdot\mathbf{u}, \nabla\cdot\mathbf{v}).$$

It is easy to see that $a(\cdot,\cdot)$ is coercive:

$$\|\mathbf{v}\|_1^2 \lesssim a(\mathbf{v},\mathbf{v}), \quad \forall\, \mathbf{v} \in (H^1(\Omega))^d. \tag{2.17}$$

We first consider a semidiscrete approximation of the system (2.13)–(2.16). We apply the CG method for the displacement and the MFMFE method [21, 44, 47] for the flow. Given finite element approximating spaces $\mathbf{V}_h \subset \mathbf{V}$, $\mathbf{Z}_h \subset \mathbf{Z}$, and $W_h \subset W$, the coupled MFMFE-CG method is: find $\mathbf{u}_h(t) \in \mathbf{V}_h$, $\mathbf{z}_h(t) \in \mathbf{Z}_h$, and $p_h(t) \in W_h$, $t \in [0,T]$, such that

$$a(\mathbf{u}_h,\mathbf{v}) - \alpha(p_h, \nabla\cdot\mathbf{v}) = (\mathbf{f},\mathbf{v}) + \langle \mathbf{t}_N, \mathbf{v}\rangle_{\Gamma_\sigma}, \quad \forall\, \mathbf{v} \in \mathbf{V}_h, \tag{2.18}$$
$$(\mathbf{K}^{-1}\mathbf{z}_h,\mathbf{q})_Q - (p_h, \nabla\cdot\mathbf{q}) = 0, \quad \forall \mathbf{q} \in \mathbf{Z}_h, \tag{2.19}$$
$$\left(\frac{\partial}{\partial t}(c_0 p_h + \alpha\nabla\cdot\mathbf{u}_h), w\right) + (\nabla\cdot\mathbf{z}_h, w) = (g,w), \forall\, w \in W_h, \tag{2.20}$$
$$\mathbf{u}_h(0) = P_h\mathbf{u}_0, \quad p_h(0) = Q_h p_0, \tag{2.21}$$

where P_h and Q_h are projection operators onto $\mathbf{V}_h$ and W_h, respectively, defined in (2.53) and (2.41), and $(\cdot,\cdot)_Q$ is a quadrature rule defined in Section 2.2.

There are two key ingredients in the MFMFE method. The first is an appropriate choice of mixed finite element spaces $\mathbf{Z}_h$ and W_h and degrees of freedom. The second is a specific choice of the numerical integration rules for $(\cdot,\cdot)_Q$ in (2.19). These two choices allow for flux variables associated with a vertex to be expressed by cell-centered pressures surrounding the vertex. We consider two quadrature rules—symmetric an nonsymmetric. The former works well on affine or smooth grids, while the latter is designed to handle rough quadrilateral or hexahedral grids.

In the next sections, we give details on the MFMFE method and the CG method on various grids.

2.1 Finite element spaces

Assume that Ω can be exactly partitioned into a union of finite elements of characteristic size h. The elements can be triangles or quadrilaterals in 2D, tetrahedra or hexahedra in 3D. Let us denote the family of partitions by $\mathcal{T}_h$ and assume that they are shape-regular and quasi-uniform [12]. This is a standard assumption in finite element analysis. It was needed in the analysis of the MEMFE method for Darcy flow in [21, 44, 47]. We utilize several auxiliary results from these papers in our analysis. We further require shape regularity of the grids for optimal approximation of the finite element space in the elasticity equation. The displacement, velocity, and pressure finite element spaces on any physical element E are defined, respectively, via the vector transformation

$$\mathbf{v} \leftrightarrow \hat{\mathbf{v}} : \mathbf{v} = \hat{\mathbf{v}} \circ F_E^{-1},$$

via the Piola transformation

$$\mathbf{q} \leftrightarrow \hat{\mathbf{q}} : \mathbf{q} = \frac{1}{J_E}\mathbb{DF}_E\hat{\mathbf{q}} \circ F_E^{-1}, \tag{2.22}$$

and via the scalar transformation

$$w \leftrightarrow \hat{w} : w = \hat{w} \circ F_E^{-1},$$

where F_E denotes a mapping from the reference element $\hat{E}$ to the physical element E, $\mathbb{DF}_E$ is the Jacobian of F_E, and J_E is its determinant. The Piola transformation preserves

the normal components of the velocity vectors. The finite element spaces $\mathbf{V}_h$, $\mathbf{Z}_h$ and W_h on $\mathcal{T}_h$ are given by

$$\begin{aligned}\mathbf{V}_h &= \left\{\mathbf{v}\in\mathbf{V}: \quad \mathbf{v}|_E \leftrightarrow \hat{\mathbf{v}},\ \hat{\mathbf{v}}\in\hat{\mathbf{V}}(\hat{E}), \quad \forall E\in\mathcal{T}_h\right\},\\ \mathbf{Z}_h &= \left\{\mathbf{q}\in\mathbf{Z}: \quad \mathbf{q}|_E \leftrightarrow \hat{\mathbf{q}},\ \hat{\mathbf{q}}\in\hat{\mathbf{Z}}(\hat{E}), \quad \forall E\in\mathcal{T}_h\right\},\\ W_h &= \left\{w\in W: \quad w|_E \leftrightarrow \hat{w},\ \hat{w}\in\hat{W}(\hat{E}), \quad \forall E\in\mathcal{T}_h\right\},\end{aligned} \tag{2.23}$$

where $\hat{\mathbf{V}}(\hat{E})$, $\hat{\mathbf{Z}}(\hat{E})$ and $\hat{W}(\hat{E})$ are finite element spaces on the reference element $\hat{E}$.

Triangular elements In the case of triangles, $\hat{E}$ is the reference triangle with vertices $\hat{\mathbf{r}}_1=(0,0)^T$, $\hat{\mathbf{r}}_2=(1,0)^T$, and $\hat{\mathbf{r}}_3=(0,1)^T$. Let $\mathbf{r}_i (i=1,2,3)$ be the corresponding vertices on the physical element. The linear mapping F_E has the form

$$F_E(\hat{r}) = \mathbf{r}_1(1-\hat{x}-\hat{y}) + \mathbf{r}_2\hat{x} + \mathbf{r}_3\hat{y}, \tag{2.24}$$

and the spaces are chosen as for displacement

$$\hat{\mathbf{V}}(\hat{E}) = (P_1(\hat{E}))^2, \tag{2.25}$$

and the lowest order BDM_1 [9] spaces for flow

$$\hat{\mathbf{Z}}(\hat{E}) = (P_1(\hat{E}))^2, \qquad \hat{W}(\hat{E}) = P_0(\hat{E}), \tag{2.26}$$

where P_k denotes the space of polynomials of degree at most k.

Convex quadrilaterals In the case of convex quadrilaterals, $\hat{E}$ is the unit square with vertices $\hat{\mathbf{r}}_1=(0,0)^T$, $\hat{\mathbf{r}}_2=(1,0)^T$, $\hat{\mathbf{r}}_3=(1,1)^T$, and $\hat{\mathbf{r}}_4=(0,1)^T$. Denote by $\mathbf{r}_i, i=1,\ldots,4$, the corresponding vertices of E. In this case, F_E is the bilinear mapping given as

$$F_E(\hat{r}) = \mathbf{r}_1(1-\hat{x})(1-\hat{y}) + \mathbf{r}_2\hat{x}(1-\hat{y}) + \mathbf{r}_3\hat{x}\hat{y} + \mathbf{r}_4(1-\hat{x})\hat{y}, \tag{2.27}$$

and the spaces are for displacement

$$\hat{\mathbf{V}}(\hat{E}) = (Q_1(\hat{E}))^2, \tag{2.28}$$

and the lowest order BDM_1 [9] spaces for flow

$$\begin{aligned}\hat{\mathbf{Z}}(\hat{E}) &= (P_1(\hat{E}))^2 + r\ \ \mathrm{curl}(\hat{x}^2\hat{y}) + s\ \ \mathrm{curl}(\hat{x}\hat{y}^2),\\ \hat{W}(\hat{E}) &= P_0(\hat{E}),\end{aligned} \tag{2.29}$$

where Q_1 denotes bilinear or trilinear polynomial spaces and r and s are real constants.

Tetrahedra In the case of tetrahedra, $\hat{E}$ is the reference tetrahedron with vertices $\hat{\mathbf{r}}_1=(0,0,0)^T$, $\hat{\mathbf{r}}_2=(1,0,0)^T$, $\hat{\mathbf{r}}_3=(0,1,0)^T$, and $\hat{\mathbf{r}}_4=(0,0,1)^T$. Let $\mathbf{r}_i\ (i=1,\ldots,4)$ be the corresponding vertices of E. The linear mapping for tetrahedra has the form

$$F_E(\hat{\mathbf{r}}) = \mathbf{r}_1(1-\hat{x}-\hat{y}-\hat{z}) + \mathbf{r}_2\hat{x} + \mathbf{r}_3\hat{y} + \mathbf{r}_4\hat{z}, \tag{2.30}$$

and the spaces are

$$\hat{\mathbf{V}}(\hat{E}) = (P_1(\hat{E}))^3, \tag{2.31}$$

for displacement and the BDM_1 spaces for flow [9]:

$$\hat{\mathbf{Z}}(\hat{E}) = (P_1(\hat{E}))^3, \qquad \hat{W}(\hat{E}) = P_0(\hat{E}). \tag{2.32}$$

Hexahedra In the case of hexahedra, $\hat{E}$ is the unit cube with vertices $\hat{\mathbf{r}}_1=(0,0,0)^T$, $\hat{\mathbf{r}}_2=(1,0,0)^T$, $\hat{\mathbf{r}}_3=(1,1,0)^T$, $\hat{\mathbf{r}}_4=(0,1,0)^T$, $\hat{\mathbf{r}}_5=(0,0,1)^T$, $\hat{\mathbf{r}}_6=(1,0,1)^T$, $\hat{\mathbf{r}}_7=(1,1,1)^T$, and $\hat{\mathbf{r}}_8=(0,1,1)^T$. Denote by $\mathbf{r}_i=(x_i,y_i,z_i)^T, i=1,\ldots,8$, the eight corresponding vertices of E. We note that the element can have nonplanar faces. In this case, F_E is a trilinear mapping given by

$$\begin{aligned}F_E(\hat{\mathbf{r}}) = {}& \mathbf{r}_1(1-\hat{x})(1-\hat{y})(1-\hat{z}) + \mathbf{r}_2\hat{x}(1-\hat{y})(1-\hat{z})\\ &+\mathbf{r}_3\hat{x}\hat{y}(1-\hat{z}) + \mathbf{r}_4(1-\hat{x})\hat{y}(1-\hat{z})\\ &+\mathbf{r}_5(1-\hat{x})(1-\hat{y})\hat{z} + \mathbf{r}_6\hat{x}(1-\hat{y})\hat{z}\\ &+\mathbf{r}_7\hat{x}\hat{y}\hat{z} + \mathbf{r}_8(1-\hat{x})\hat{y}\hat{z},\end{aligned} \tag{2.33}$$

and the spaces are defined by

$$\hat{\mathbf{V}}(\hat{E}) = (Q_1(\hat{E}))^3, \tag{2.34}$$

for displacement and by enhancing the BDDF_1 spaces [21] for flow:

$$\begin{aligned}\hat{\mathbf{Z}}(\hat{E}) = {}& \mathrm{BDDF}_1(\hat{E}) + s_2\mathrm{curl}(0,0,\hat{x}^2\hat{z})^T\\ &+s_3\mathrm{curl}(0,0,\hat{x}^2\hat{y}\hat{z})^T + t_2\mathrm{curl}(\hat{x}\hat{y}^2,0,0)^T\\ &+t_3\mathrm{curl}(\hat{x}\hat{y}^2\hat{z},0,0)^T + w_2\mathrm{curl}(0,\hat{y}\hat{z}^2,0)^T\\ &+w_3\mathrm{curl}(0,\hat{x}\hat{y}\hat{z}^2,0)^T,\\ \hat{W}(\hat{E}) = {}& P_0(\hat{E}),\end{aligned} \tag{2.35}$$

where the $\mathrm{BDDF}_1(\hat{E})$ space is defined as [8]:

$$\begin{aligned}\mathrm{BDDF}_1(\hat{E}) = {}& (P_1(\hat{E}))^3 + s_0\mathrm{curl}(0,0,\hat{x}\hat{y}\hat{z})^T\\ &+s_1\mathrm{curl}(0,0,\hat{x}\hat{y}^2)^T + t_0\mathrm{curl}(\hat{x}\hat{y}\hat{z},0,0)^T,\\ &+t_1\mathrm{curl}(\hat{y}\hat{z}^2,0,0)^T + w_0\mathrm{curl}(0,\hat{x}\hat{y}\hat{z},0)^T\\ &+w_1\mathrm{curl}(0,\hat{x}^2\hat{z},0)^T.\end{aligned} \tag{2.36}$$

In above equations, $s_i, t_i, w_i (i=0,\ldots,3)$ are real constants.

In all cases, the degrees of freedom (DOF) for displacements are chosen as Lagrangian nodal point values. The velocity DOF are chosen to be the normal components at n points on each face where n is the number of vertices of that face. We choose these points to be the vertices. The dimension of the space is dn_v, where d is the dimension and n_v is the number of vertices in E. Note that the original BDDF_1 spaces have only three DOF on square faces. These spaces have been enhanced in [21] to have 4 DOF on square faces. This special choice is needed in the reduction to a cell-centered pressure stencil in a pure Darcy flow problem as described later in this section. In addition, the normal

components of the velocity vectors on the faces (edges) are preserved [10], under the Piola transformation (2.22):

$$(\nabla \cdot \mathbf{q}, w)_E = (\hat{\nabla} \cdot \hat{\mathbf{q}}, \hat{w})_{\hat{E}} \text{ and } \langle \mathbf{q} \cdot \mathbf{n}_e, w \rangle_e = \langle \hat{\mathbf{q}} \cdot \hat{\mathbf{n}}_{\hat{e}}, \hat{w} \rangle_{\hat{e}}, \tag{2.37}$$

which is needed for an $H(\mathrm{div}; \Omega)$-conforming velocity space as required by (2.23).

Recall the projection operators in the space $\mathbf{Z}_h$ and W_h. The operator $\hat{\Pi} : (H^1(\hat{E}))^d \to \hat{\mathbf{Z}}(\hat{E})$ is defined locally on each element by

$$\langle (\hat{\Pi}\hat{\mathbf{q}} - \hat{\mathbf{q}}) \cdot \hat{\mathbf{n}}_{\hat{e}}, \hat{q}_1 \rangle_{\hat{e}} = 0, \quad \forall \hat{e} \subset \partial \hat{E}, \tag{2.38}$$

where $\hat{q}_1 \in P_1(\hat{e})$ for the case of the unit square (or simplices) $\hat{E}$, and $\hat{q}_1 \in Q_1(\hat{e})$ for the case of the unit cube $\hat{E}$. The global operator $\Pi : \mathbf{Z} \cap (H^1(\Omega))^d \to \mathbf{Z}_h$ on each element E is defined by the Piola transformation:

$$\Pi \mathbf{q} \leftrightarrow \widehat{\Pi \mathbf{q}}, \quad \widehat{\Pi \mathbf{q}} = \hat{\Pi}\hat{\mathbf{q}}. \tag{2.39}$$

Furthermore, $\Pi \mathbf{q} \cdot \mathbf{n}$ is continuous across element interfaces and

$$(\nabla \cdot (\Pi \mathbf{q} - \mathbf{q}), w) = 0, \quad \forall w \in W_h. \tag{2.40}$$

Let $\hat{Q}$ be the $L^2(\hat{E})$-orthogonal projection onto $\hat{W}(\hat{E})$, satisfying for any $\hat{\varphi} \in L^2(\hat{E})$,

$$(\hat{\varphi} - \hat{Q}\,\hat{\varphi}, \hat{w})_{\hat{E}} = 0, \quad \forall\, \hat{w} \in \hat{W}(\hat{E}).$$

Let $Q_h : L^2(\Omega) \to W_h$ be the projection operator satisfying for any $\varphi \in L^2(\Omega)$,

$$Q_h \varphi = \hat{Q}\hat{\varphi} \circ F_E^{-1} \quad \text{on all } E. \tag{2.41}$$

It is easy to see that, due to (2.37),

$$(\varphi - Q_h \varphi, \nabla \cdot \mathbf{q}) = 0, \quad \forall\, \mathbf{q} \in \mathbf{Z}_h. \tag{2.42}$$

2.2 A quadrature rule

We first introduce some notation on the element geometry. A quadrilateral in 2D or a hexahedral face in 3D with vertices $\mathbf{r}_1$, $\mathbf{r}_2$, $\mathbf{r}_3$, and $\mathbf{r}_4$ (numbered counter clockwise) is called an h^2-parallelogram if

$$|\mathbf{r}_{34} - \mathbf{r}_{21}|_{\mathbb{R}^d} \lesssim h^2.$$

A hexahedron is called an h^2-parallelepiped when all of its faces are h^2-parallelograms. We refer to grids of such elements as h^2-perturbed grids. It holds for such grids that $|\mathbb{DF}_E|_{1,\infty,\hat{E}} \lesssim h^2$. We employ a symmetric quadrature rule on affine and h^2-perturbed grids and a nonsymmetric rule on general quadrilaterals and hexahedra.

The integration on a physical element is performed by mapping to the reference element and choosing a quadrature rule on $\hat{E}$. Using the Piola transformation, we write $(\mathbf{K}^{-1}\cdot, \cdot)$ in (2.14) as

$$\begin{aligned}(\mathbf{K}^{-1}\mathbf{q}, \mathbf{s})_E &= \left(\frac{1}{J_E}\mathbb{DF}_E^T \mathbf{K}^{-1}(F_E(\hat{x}))\mathbb{DF}_E \hat{\mathbf{q}}, \hat{\mathbf{s}}\right)_{\hat{E}} \\ &\equiv (\mathcal{M}_E \hat{\mathbf{q}}, \hat{\mathbf{s}})_{\hat{E}},\end{aligned}$$

where

$$\mathcal{M}_E = \frac{1}{J_E}\mathbb{DF}_E^T \mathbf{K}^{-1}(F_E(\hat{x}))\mathbb{DF}_E. \tag{2.43}$$

Define a perturbed $\widetilde{\mathcal{M}}_E$ as

$$\widetilde{\mathcal{M}}_E = \frac{1}{J_E}\mathbb{DF}_E^T \left(\hat{\mathbf{r}}_{c,\hat{E}}\right) \overline{\mathbf{K}}_E^{-1} \mathbb{DF}_E, \tag{2.44}$$

where $\hat{\mathbf{r}}_{c,\hat{E}}$ is the centroid of $\hat{E}$ and $\overline{\mathbf{K}}_E$ denotes the mean of $\mathbf{K}$ on E. In addition, denote the trapezoidal rule on $\hat{E}$ by $\mathrm{Trap}(\cdot, \cdot)_{\hat{E}}$:

$$\mathrm{Trap}(\hat{\mathbf{q}}, \hat{\mathbf{s}})_{\hat{E}} \equiv \frac{|\hat{E}|}{k} \sum_{i=1}^{k} \hat{\mathbf{q}}(\hat{\mathbf{r}}_i) \cdot \hat{\mathbf{s}}(\hat{\mathbf{r}}_i), \tag{2.45}$$

where $\{\hat{\mathbf{r}}_i\}_{i=1}^k$ are the vertices of $\hat{E}$.

The symmetric quadrature rule is based on the original $\mathcal{M}_E$ while the nonsymmetric one is based on the perturbed $\widetilde{\mathcal{M}}_E$:

$$(K^{-1}\mathbf{q}, \mathbf{s})_{Q,E} \equiv \begin{cases} \mathrm{Trap}(\mathcal{M}_E \hat{\mathbf{q}}, \hat{\mathbf{s}})_{\hat{E}} = \frac{|\hat{E}|}{k} \sum_{i=1}^{k} \mathcal{M}_E(\hat{\mathbf{r}}_i)\hat{\mathbf{q}}(\hat{\mathbf{r}}_i) \cdot \hat{\mathbf{s}}(\hat{\mathbf{r}}_i), & \text{symmetric,} \\ \mathrm{Trap}(\widetilde{\mathcal{M}}_E \hat{\mathbf{q}}, \hat{\mathbf{s}})_{\hat{E}} = \frac{|\hat{E}|}{k} \sum_{i=1}^{k} \widetilde{\mathcal{M}}_E(\hat{\mathbf{r}}_i)\hat{\mathbf{q}}(\hat{\mathbf{r}}_i) \cdot \hat{\mathbf{s}}(\hat{\mathbf{r}}_i), & \text{nonsymmetric.} \end{cases} \tag{2.46}$$

Mapping back to the physical element E, we have the quadrature rule on E as

$$(K^{-1}\mathbf{q}, \mathbf{s})_{Q,E} = \begin{cases} \frac{1}{k} \sum_{i=1}^{k} J_E(\hat{\mathbf{r}}_i)\mathbf{K}_E^{-1}\mathbf{q}(\mathbf{r}_i) \cdot \mathbf{s}(\mathbf{r}_i), & \text{symmetric,} \\ \frac{1}{k} \sum_{i=1}^{k} J_E(\hat{\mathbf{r}}_i) \left(\mathbb{DF}_E^{-1}\right)^T (\mathbf{r}_i)\mathbb{DF}_E^T \left(\hat{\mathbf{r}}_{c,\hat{E}}\right) \overline{\mathbf{K}}_E^{-1}\mathbf{q}(\mathbf{r}_i) \cdot \mathbf{s}(\mathbf{r}_i), & \text{nonsymmetric.} \end{cases} \tag{2.47}$$

We call the method symmetric or nonsymmetric MFMFE method depending on the choice of quadrature rule. On affine or h^2-perturbed grids, both the symmetric and the nonsymmetric MFMFE methods give first-order accurate velocities and pressures, as well as second-order accurate face fluxes and pressures at the cell centers [21, 44, 47]. On general quadrilateral and hexahedral grids, the convergence of the symmetric MFMFE method can deteriorate while the nonsymmetric MFMFE method still gives first-order accuracy [47]. This is due to the fact that the nonsymmetric quadrature rule satisfies some critical properties on the physical elements, see Lemma 3.3 and Lemma 3.4. On affine grids, the two quadrature rules in (2.46) are the same if the tensor $\mathbf{K}$ is constant in each element, since the Jacobian is a constant matrix. The nonsymmetric quadrature rule was originally proposed in [24] for quadrilateral grids.

The global quadrature rule on Ω is then given as

$$(\mathbf{K}^{-1}\mathbf{q}, \mathbf{s})_Q \equiv \sum_{E\in\mathcal{T}_h} (\mathbf{K}^{-1}\mathbf{q}, \mathbf{s})_{Q,E}.$$

Note that

$$(\mathbf{K}^{-1}\mathbf{q}, \mathbf{s})_Q = \sum_{E\in\mathcal{T}_h} (\mathbf{K}^{-1}\mathbf{q}, \mathbf{s})_{Q,E} = \sum_{c\in\mathcal{C}_h} \mathbf{s}_c^T \mathbf{M}_c \mathbf{q}_c, \quad (2.48)$$

where $\mathcal{C}_h$ denotes the set of corner or vertex points in $\mathcal{T}_h$, $\mathbf{q}_c := \{(\mathbf{q}\cdot\mathbf{n}_e)(\mathbf{r}_c)\}_{e=1}^{n_c}$, $\mathbf{r}_c$ is the coordinate vector of point c, and n_c is the number of faces (or edges in 2D) that share the vertex point c.

Lemma 2.1 ([21, 44]) *The symmetric bilinear form $(\mathbf{K}^{-1}\cdot,\cdot)_Q$ is coercive in $\mathbf{Z}_h$ and induces a norm in $\mathbf{Z}_h$ equivalent to the L^2-norm:*

$$(\mathbf{K}^{-1}\mathbf{q}, \mathbf{q})_Q \eqsim \|\mathbf{q}\|^2, \quad \forall\, \mathbf{q}\in\mathbf{Z}_h. \quad (2.49)$$

The analysis of the nonsymmetric MFMFE method requires some additional assumptions.

Lemma 2.2 ([47]) *Assume that $\mathbf{M}_c$ is uniformly positive definite for all $c\in\mathcal{C}_h$:*

$$h^d \boldsymbol{\xi}^T\boldsymbol{\xi} \lesssim \boldsymbol{\xi}^T\mathbf{M}_c\boldsymbol{\xi}, \quad \forall\boldsymbol{\xi}\in\mathbb{R}^{n_c}. \quad (2.50)$$

Then the nonsymmetric bilinear form $(\mathbf{K}^{-1}\cdot,\cdot)_Q$ is coercive in $\mathbf{Z}_h$ and satisfies (2.49). If in addition

$$\boldsymbol{\xi}^T\mathbf{M}_c^T\mathbf{M}_c\boldsymbol{\xi} \lesssim h^{2d}\boldsymbol{\xi}^T\boldsymbol{\xi}, \quad \forall\boldsymbol{\xi}\in\mathbb{R}^{n_c}, \quad (2.51)$$

then the following Cauchy-Schwarz type inequality holds:

$$(\mathbf{K}^{-1}\mathbf{q}, \mathbf{s})_Q \lesssim \|\mathbf{q}\|\|\mathbf{s}\| \quad \forall\mathbf{q},\mathbf{s}\in\mathbf{Z}_h, \quad (2.52)$$

2.3 Reduction to a cell-centered pressure system in the flow problem

The choice of trapezoidal quadrature rule implies that on each element, the velocity degrees of freedom associated with a vertex become decoupled from the rest of the degrees of freedom. As a result, the assembled velocity mass matrix in (2.19) has a block-diagonal structure with one block per grid vertex. The dimension of each block equals the number of velocity DOF associated with the vertex. For example, this dimension is 12 for logically rectangular hexahedral grids, see Fig. 1. Inverting each local block in the mass matrix in (2.19) allows for expressing the velocity DOF associated with a vertex in terms of the pressures at the centers of the elements that share the vertex (there are eight such elements in Fig. 1). Substituting these expressions into the mass conservation equation (2.20) leads to a cell-centered system for the pressures. The stencil is 9 or 27 points on logically rectangular quadrilateral or hexahedral grids, respectively. The local linear systems and the resulting global pressure system are positive definite and therefore invertible for the symmetric MFMFE method and, under a mild restriction on the shape regularity of the grids and/or the anisotropy of the permeability, for the nonsymmetric MFMFE method; see (2.50) below. The reader is referred to [21, 44, 46, 47] for further details on the reduction to a cell-centered pressure system.

2.4 Some preliminaries

In the analysis we, will make use of the following finite element interpolants or projections. Let P_h be the elliptic elasticity projection in $\mathbf{V}_h$ satisfying

$$a(P_h\mathbf{u}-\mathbf{u}, \mathbf{v}) = 0, \quad \forall\mathbf{v}\in\mathbf{V}_h. \quad (2.53)$$

The finite element elliptic elasticity theory [12], also [4, 29], gives

$$\|\mathbf{u}-P_h\mathbf{u}\|_1 \lesssim h\|\mathbf{u}\|_2, \quad (2.54)$$

$$\|(\mathbf{u}-P_h\mathbf{u})_t\|_1 \lesssim h\|\mathbf{u}_t\|_2. \quad (2.55)$$

It has been shown in [5, 21, 43] that on general quadrilaterals and h^2-parallelepipeds,

$$\|\mathbf{q}-\Pi\mathbf{q}\| \lesssim h\|\mathbf{q}\|_1. \quad (2.56)$$

However, on general hexahedra, it only holds that [16, 33, 40]

$$\|\mathbf{q}-\Pi\mathbf{q}\| = O(1). \quad (2.57)$$

On simplices, we have optimal interpolation error estimates [9]:

$$\|\mathbf{q}-\Pi\mathbf{q}\| \lesssim h^r\|\mathbf{q}\|_r, \quad r=1,2. \quad (2.58)$$

Using a scaling argument and the Bramble-Hilbert lemma [12], it can be shown that

$$\|\varphi - Q_h\varphi\| \lesssim h\|\varphi\|_1, \quad (2.59)$$

$$\|(\varphi - Q_h\varphi)_t\| \lesssim h\|\varphi_t\|_1. \quad (2.60)$$

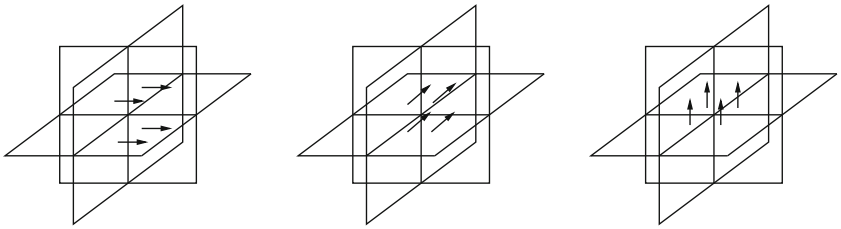

Fig. 1 Interactions of the velocity degrees of freedom in the MFMFE method

In the analysis, we will use the following well-known estimates [7]. There exists $s^1 \in P_1(E)$ such that

$$\|p - s^1\|_{j,E} \lesssim h^{2-j}\|p\|_{2,E}, \quad j = 0, 1, \tag{2.61}$$

and

$$\|p - s^1\|_E \lesssim h\|p\|_{1,E}. \tag{2.62}$$

We also have [12]

$$\|\mathbf{K} - \overline{\mathbf{K}}_E\|_E \lesssim h\|\mathbf{K}\|_{1,E}. \tag{2.63}$$

Lemma 2.3 ([47]) *For all* $\mathbf{q} \in (H^1(E))^d$,

$$\|\Pi\mathbf{q}\|_E \lesssim \|\mathbf{q}\|_E + h|\mathbf{q}|_{1,E}. \tag{2.64}$$

In the analysis, we will require a similar projection operator onto the lowest order Raviart-Thomas velocity space [34, 39]. The RT_0 spaces are defined on the unit cube as

$$\hat{\mathbf{Z}}^R(\hat{E}) = \begin{pmatrix} \alpha_1 + \beta_1\hat{x} \\ \alpha_2 + \beta_2\hat{y} \\ \alpha_3 + \beta_3\hat{z} \end{pmatrix}, \qquad \hat{W}^R(\hat{E}) = P_0(\hat{E}), \tag{2.65}$$

and on the unit square as

$$\hat{\mathbf{Z}}^R(\hat{E}) = \begin{pmatrix} \alpha_1 + \beta_1\hat{x} \\ \alpha_2 + \beta_2\hat{y} \end{pmatrix}, \qquad \hat{W}^R(\hat{E}) = P_0(\hat{E}). \tag{2.66}$$

Here, $\alpha_i$and $\beta_i (i = 1, 2, 3)$ are real constants. On simplicies,

$$\hat{\mathbf{Z}}^R(\hat{E}) = (P_1(\hat{E}))^d, \quad \hat{W}^R(\hat{E}) = P_0(\hat{E}). \tag{2.67}$$

In all cases, $\hat{\nabla} \cdot \hat{\mathbf{Z}}^R(\hat{E}) = \hat{W}^R(\hat{E})$ and $\hat{\mathbf{v}} \cdot \hat{\mathbf{n}}_{\hat{e}} \in P_0(\hat{e})$. The degrees of freedom of $\hat{\mathbf{V}}^R(\hat{E})$ are chosen to be the constant values of $\hat{\mathbf{v}} \cdot \hat{\mathbf{n}}_{\hat{e}}$ on all faces (or edges) of $\hat{E}$. The projection operator $\hat{\Pi}_R : (H^1(\hat{E}))^d \to \hat{\mathbf{Z}}_R(\hat{E})$ satisfies

$$\langle(\hat{\Pi}_R\hat{\mathbf{q}} - \hat{\mathbf{q}}) \cdot \hat{\mathbf{n}}_{\hat{e}}, \hat{q}_0\rangle_{\hat{e}} = 0, \quad \forall \hat{e} \subset \partial\hat{E}, \quad \forall \hat{q}_0 \in P_0(\hat{E}). \tag{2.68}$$

The spaces $\mathbf{Z}_h^R$ and W_h^R on $\mathcal{T}_h$ and the projection operator $\Pi_R : (H^1(\Omega))^d \to \mathbf{V}_h^R$ are defined similarly to the case of $\mathbf{V}_h$ and W_h. By definition, we have

$$\mathbf{Z}_h^R \subset \mathbf{Z}_h, \qquad W_h^R = W_h. \tag{2.69}$$

The projection operator Π_R satisfies

$$\|\Pi_R\mathbf{q}\| \lesssim \|\mathbf{q}\|, \quad \forall \mathbf{q} \in \mathbf{Z}_h, \tag{2.70}$$

and

$$(\nabla \cdot (\Pi_R\mathbf{q} - \mathbf{q}), w) = 0, \quad \forall w \in W_h^R, \tag{2.71}$$

which implies

$$\nabla \cdot \mathbf{q} = \nabla \cdot \Pi_R\mathbf{q}, \quad \forall \mathbf{q} \in \mathbf{Z}_h. \tag{2.72}$$

3 Convergence results of the MFMFE method on pure flow problems

In this section, we state some known convergence results for the MFMFE method applied to the pure Darcy flow problem

$$\left(\mathbf{K}^{-1}\mathbf{z}_h, \mathbf{q}\right)_Q - (p_h, \nabla\cdot\mathbf{q}) = 0, \quad \forall \mathbf{q} \in \mathbf{Z}_h, \tag{3.73}$$

$$(\nabla\cdot\mathbf{z}_h, w) = (g, w), \qquad \forall\, w \in W_h. \tag{3.74}$$

3.1 Convergence of the symmetric MFMFE method

Let $W_{\mathcal{T}_h}^{k,\infty}$ consist of functions ϕ such that $\phi|_E \in W^{k,\infty}(E)$ for all $E \in \mathcal{T}_h$.

Theorem 3.1 ([21, 44]) *On simplicial grids,* h^2*-parallelograms, and* h^2*-parallelepipeds, if* $\mathbf{K}^{-1} \in W_{\mathcal{T}_h}^{1,\infty}$*, then, the velocity* $\mathbf{z}_h$ *and the pressure* p_h *of the symmetric MFMFE method* (3.73)–(3.74) *satisfy*

$$\|\mathbf{z} - \mathbf{z}_h\| \lesssim h\|\mathbf{z}\|_1, \tag{3.75}$$

$$\|\nabla \cdot (\mathbf{z} - \mathbf{z}_h)\| \lesssim h\|\nabla \cdot \mathbf{z}\|_1, \tag{3.76}$$

$$\|p - p_h\| \lesssim h(\|\mathbf{z}\|_1 + \|p\|_1). \tag{3.77}$$

3.2 Convergence of the nonsymmetric MFMFE method

On simplicial grids, h^2-parallelograms, and h^2-parallelepipeds, the nonsymmetric MFMFE method has the same order of accuracy as the symmetric method. In addition, the nonsymmetric method has first-order convergence for the velocity and pressure on general quadrilaterals and for the

face flux and pressure on general hexahedra with nonplanar faces.

Theorem 3.2 ([47]) *Let* $\mathbf{K} \in W^{1,\infty}_{\mathcal{T}_h}$ *and* $\mathbf{K}^{-1} \in W^{0,\infty}(\Omega)$. *If* (2.50) *and* (2.51) *hold, then the velocity* $\mathbf{z}_h$ *and the pressure* p_h *of the nonsymmetric MFMFE method* (3.73)–(3.74) *satisfy*

$$\|\Pi \mathbf{z} - \mathbf{z}_h\| + \|Q_h p - p_h\| \lesssim h(|\mathbf{z}|_1 + \|p\|_2). \tag{3.78}$$

This result further implies convergence of the computed normal velocity to the true normal velocity on the element faces. First, define a norm for vectors in Ω based on the normal components on the faces of $\mathcal{T}_h$:

$$\|\mathbf{q}\|^2_{\mathcal{F}_h} := \sum_{E\in\mathcal{T}_h} \sum_{e\in\partial E} \frac{|E|}{|e|} \|\mathbf{q}\cdot\mathbf{n}_e\|^2_e, \tag{3.79}$$

where $|E|$ is the volume of E and $|e|$ is the area of e. This norm gives an appropriate scaling of $|\Omega|^{1/2}$ for a unit vector.

Theorem 3.3 ([47]) *Let* $\mathbf{K} \in W^{1,\infty}_{\mathcal{T}_h}$ *and* $\mathbf{K}^{-1} \in W^{0,\infty}(\Omega)$. *If* (2.50) *and* (2.51) *hold, then the velocity* $\mathbf{z}_h$ *of the nonsymmetric MFMFE method* (3.73)–(3.74) *satisfies*

$$\|\mathbf{z} - \mathbf{z}_h\|_{\mathcal{F}_h} \lesssim h(\|\mathbf{z}\|_1 + \|p\|_2). \tag{3.80}$$

3.3 Auxiliary lemmas for the MFMFE method

We give several results from earlier papers on the MFMFE method for Darcy that are utilized in our analysis.

Lemma 3.1 ([21, 44]) *For the symmetric method on* h^2*-parallelograms and* h^2*-parallelepipeds, if* $\mathbf{K}^{-1} \in W^{1,\infty}_{\mathcal{T}_h}$, *then for all* $\mathbf{q} \in \mathbf{Z}_h$,

$$|(\mathbf{K}^{-1}\Pi\mathbf{z}, \mathbf{q} - \Pi_R\mathbf{q})_Q| \lesssim h\|\mathbf{z}\|_1\|\mathbf{q}\|. \tag{3.81}$$

Lemma 3.2 ([21, 44]) *For the symmetric method on* h^2*-parallelograms and* h^2*-parallelepipeds, if* $\mathbf{K}^{-1} \in W^{1,\infty}_{\mathcal{T}_h}$, *then for all* $\mathbf{q} \in \mathbf{Z}_h$ *and for all* $\mathbf{s} \in \mathbf{Z}^R_h$

$$\begin{aligned}|\sigma(\mathbf{K}^{-1}\mathbf{q}, \mathbf{s})| &:= |(\mathbf{K}^{-1}\mathbf{q}, \mathbf{s}) - (\mathbf{K}^{-1}\mathbf{q}, \mathbf{s})_Q| \\ &\lesssim \sum_{E\in\mathcal{T}_h} h\|K^{-1}\|_{1,\infty,E}\|\mathbf{q}\|_{1,E}\|\mathbf{s}\|_E. \end{aligned}\tag{3.82}$$

Furthermore, the above bound holds on simplices for all $\mathbf{s} \in \mathbf{Z}_h$.

Lemma 3.3 ([47]) *For the nonsymmetric method on general quadrilateral or hexahedral elements, for any constant vector* $\mathbf{s}_0$ *on* E *and for all* $\mathbf{q} \in \mathbf{Z}_h(E)$,

$$\left(\mathbf{K}^{-1}\mathbf{s}_0, \mathbf{q} - \Pi_R\mathbf{q}\right)_{Q,E} = 0. \tag{3.83}$$

Lemma 3.4 ([47]) *For the nonsymmetric method on general quadrilateral or hexahedral elements, for any constant vector* $\mathbf{s}_0$ *on* E *and* $\mathbf{q} \in \mathbf{Z}^R_h(E)$,

$$\left(\mathbf{K}^{-1}\mathbf{s}_0, \mathbf{q}\right)_{Q,E} = \left(\overline{\mathbf{K}}_E^{-1}\mathbf{s}_0, \mathbf{q}\right)_E. \tag{3.84}$$

Lemma 3.5 ([47]) *On general quadrilateral or hexahedral elements, for any constant vector* $\mathbf{s}_0$ *on* E,

$$\forall\, e \subset \partial E, \quad \Pi\mathbf{s}_0\cdot\mathbf{n}_e = \mathbf{s}_0\cdot\mathbf{n}_e. \tag{3.85}$$

4 Convergence of the semidiscrete poroelasticity scheme

We begin with a well-posedness result.

Lemma 4.1 *The system* (2.18)–(2.20) *has a unique solution.*

Proof For any fixed t this is a square finite dimensional system and existence is equivalent to uniqueness. Take all problem data to be zero. Take $\mathbf{v} = \mathbf{u}_{h,t}$, $\mathbf{q} = \mathbf{z}_h$, and $w = p_h$ to conclude that

$$\frac{1}{2}\frac{\partial}{\partial t}a(\mathbf{u}_h, \mathbf{u}_h) + \frac{1}{2}\frac{\partial}{\partial t}(c_0 p_h, p_h) + \left(\mathbf{K}^{-1}\mathbf{z}_h, \mathbf{z}_h\right)_Q = 0.$$

Integrating the above equation from 0 to t implies, using (2.17) and (2.49), that $\mathbf{u}_h(t) = \mathbf{z}_h(t) = p_h(t) = 0$. □

The convergence analysis applies to simplices, h^2-parallelograms, and h^2-parallelepipeds in the case of the symmetric MFMFE method and in addition to general quadrilaterals and hexahedra in the case of the nonsymmetric MFMFE method.

Subtracting (2.18)–(2.20) from (2.13)–(2.15) gives the error equations

$$a(P_h\mathbf{u} - \mathbf{u}_h, \mathbf{v}) - \alpha(Q_h p - p_h, \nabla\cdot\mathbf{v}) = T_1(\mathbf{v}),\ \forall \mathbf{v} \in \mathbf{V}_h, \tag{4.1}$$

$$\left(\mathbf{K}^{-1}(\Pi\mathbf{z} - \mathbf{z}_h), \mathbf{q}\right)_Q - (Q_h p - p_h, \nabla\cdot\mathbf{q}) = T_2(\mathbf{q}),\ \forall \mathbf{q} \in \mathbf{Z}_h, \tag{4.2}$$

$$\begin{aligned}&(c_0(Q_h p - p_h)_t + \alpha\nabla\cdot(P_h\mathbf{u} - \mathbf{u}_h)_t, w) + (\nabla\cdot(\Pi\mathbf{z} - \mathbf{z}_h), w) \\ &\qquad = T_3(w),\ \forall w \in W_h,\end{aligned} \tag{4.3}$$

where the right hand sides of (4.1)–(4.2) are

$$T_1(\mathbf{v}) := \alpha(p - Q_h p, \nabla\cdot\mathbf{v}), \tag{4.4}$$
$$T_2(\mathbf{q}) := -(\mathbf{K}^{-1}\mathbf{z}, \mathbf{q}) + (\mathbf{K}^{-1}\Pi\mathbf{z}, \mathbf{q})_Q, \tag{4.5}$$
$$T_3(w) := (\alpha\nabla\cdot(P_h\mathbf{u} - \mathbf{u})_t, w). \tag{4.6}$$

Lemma 4.2 *In the case of the symmetric quadrature rule, for all* $\mathbf{q} \in \mathbf{Z}_h$,

$$|T_2(\mathbf{q})| \lesssim h\|\mathbf{z}\|_1\|\mathbf{q}\|. \tag{4.7}$$

In the case of the nonsymmetric quadrature rule, for all $\mathbf{q} \in \mathbf{Z}_h$,

$$|T_2(\mathbf{q})| \lesssim h(\|p\|_2 + |\mathbf{z}|_1)\|\mathbf{q}\|. \tag{4.8}$$

Proof We first present the argument in the case of the symmetric quadrature rule on h^2-parallelograms and h^2-parallelepipeds. In this case, the quadrature error can be bounded when one of the arguments is in the RT_0 space $\mathbf{Z}_h^R$, thus we need to project the test function using Π_R. We rewrite $T_2(\mathbf{q})$ as

$$\begin{aligned} T_2(\mathbf{q}) &= -\left(\mathbf{K}^{-1}\mathbf{z}, \mathbf{q} - \Pi_R\mathbf{q}\right) - \left(\mathbf{K}^{-1}(\mathbf{z} - \Pi\mathbf{z}), \Pi_R\mathbf{q}\right) \\ &\quad - \left(\mathbf{K}^{-1}\Pi\mathbf{z}, \Pi_R\mathbf{q}\right) + \left(\mathbf{K}^{-1}\Pi\mathbf{z}, \Pi_R\mathbf{q}\right)_Q \\ &\quad + \left(\mathbf{K}^{-1}\Pi\mathbf{z}, \mathbf{q} - \Pi_R\mathbf{q}\right)_Q \\ &\equiv J_1 + J_2 + J_3 + J_4 + J_5. \end{aligned} \tag{4.9}$$

Taking $\mathbf{q} - \Pi_R\mathbf{q}$ as a test function (2.14) and using the fact that $\nabla\cdot(\mathbf{q} - \Pi_R\mathbf{q}) = 0$, gives

$$J_1 = 0. \tag{4.10}$$

The second term in (4.9) can be bounded as

$$|J_2| = \left|\left(\mathbf{K}^{-1}(\mathbf{z} - \Pi\mathbf{z}), \Pi_R\mathbf{q}\right)\right| \lesssim h\|\mathbf{K}^{-1}\|_{0,\infty}\|\mathbf{z}\|_1\|\mathbf{q}\|, \tag{4.11}$$

by the interpolation bounds (2.56) and (2.70). The third and fourth term in (4.9) are the quadrature error, which can be bounded as

$$|J_3 + J_4| \lesssim h\|\mathbf{K}^{-1}\|_{1,\infty}\|\mathbf{z}\|_1\|\mathbf{q}\|, \tag{4.12}$$

using Lemma 3.2. For the fifth term in (4.9), we have

$$|J_5| \lesssim h\|\mathbf{K}^{-1}\|_{0,\infty}\|\mathbf{z}\|_1\|\mathbf{q}\|, \tag{4.13}$$

which follows from Lemma 3.1. Combining (4.9)–(4.13) implies

$$|T_2(\mathbf{q})| \lesssim h\|\mathbf{K}^{-1}\|_{1,\infty}\|\mathbf{z}\|_1\|\mathbf{q}\|. \tag{4.14}$$

In the case of the symmetric quadrature rule on simplices, the quadrature error can be bounded when both arguments are in $\mathbf{Z}_h$, which simplifies the argument. We rewrite $T_2(\mathbf{q})$ as

$$\begin{aligned} T_2(\mathbf{q}) &= -(\mathbf{K}^{-1}(\mathbf{z} - \Pi\mathbf{z}), \mathbf{q}) - (\mathbf{K}^{-1}\Pi\mathbf{z}, \mathbf{q}) + (\mathbf{K}^{-1}\Pi\mathbf{z}, \mathbf{q})_Q \\ &\equiv \tilde{J}_2 + \tilde{J}_3 + \tilde{J}_4. \end{aligned}$$

Note that terms J_1 and J_5 are not present. The term $\tilde{J}_2$ is bounded the same way as the term J_2 in (4.11). The quadrature error $\tilde{J}_3 + \tilde{J}_4$ is bounded as in (4.12), using Lemma 3.2. This completes the proof on simplices.

In the case of the nonsymmetric quadrature rule, using (2.14) and integration by parts, we rewrite $T_2(\mathbf{q})$ as

$$\begin{aligned} T_2(\mathbf{q}) &= (\nabla p, \mathbf{q}) + \sum_{E\in\mathcal{T}_h}\left(\mathbf{K}^{-1}\Pi(\mathbf{z} + \overline{\mathbf{K}}_E\nabla s^1), \mathbf{q}\right)_{Q,E} \\ &\quad - \sum_{E\in\mathcal{T}_h}\left(\mathbf{K}^{-1}\Pi\overline{\mathbf{K}}_E\nabla s^1, \mathbf{q}\right)_{Q,E} \\ &\equiv I_1 + I_2 + I_3 \end{aligned} \tag{4.15}$$

where s^1 is defined in (2.61). By Lemmas 3.5, 3.3, and 3.4, the term I_3 can be written as

$$\begin{aligned} -I_3 &= \left(\mathbf{K}^{-1}\Pi\overline{\mathbf{K}}_E\nabla s^1, \mathbf{q}\right)_{Q,E} \\ &= \left(\mathbf{K}^{-1}\overline{\mathbf{K}}_E\nabla s^1, \mathbf{q}\right)_{Q,E} \\ &= \left(\mathbf{K}^{-1}\overline{\mathbf{K}}_E\nabla s^1, \Pi_R\mathbf{q}\right)_{Q,E} \\ &= \left(\nabla s^1, \Pi_R\mathbf{q}\right)_E. \end{aligned} \tag{4.16}$$

Then using the fact that $(\nabla p, \mathbf{q} - \Pi_R\mathbf{q}) = -(p, \nabla\cdot(\mathbf{q} - \Pi_R\mathbf{q})) = 0$, we have

$$\begin{aligned} |I_1 + I_3| &= \left|\sum_{E\in\mathcal{T}_h}\left(\nabla\left(p - s^1\right), \Pi_R\mathbf{q}\right)_E\right| \\ &\lesssim \sum_{E\in\mathcal{T}_h}\|\nabla(p - s^1)\|_E\|\Pi_R\mathbf{q}\|_E \\ &\lesssim h\|p\|_2\|\mathbf{q}\|, \end{aligned} \tag{4.17}$$

where we have used (2.61) and (2.70). From (2.61) and (2.63),

$$\begin{aligned} \|\mathbf{z} + \overline{\mathbf{K}}_E\nabla s^1\|_E &\le \|(\mathbf{K} - \overline{\mathbf{K}}_E)\nabla p\|_E + \|\overline{\mathbf{K}}_E\nabla(p - s^1)\|_E \\ &\lesssim h(\|\nabla p\|_E + \|p\|_{2,E}) \lesssim h\|p\|_{2,E}. \end{aligned} \tag{4.18}$$

Then I_2 can be bounded as

$$
\begin{aligned}
|I_2| &\lesssim \sum_{E\in\mathcal{T}_h} \|\Pi\left(\mathbf{z}+\overline{\mathbf{K}}_E\nabla s^1\right)\|_E\|\mathbf{q}\|_E \\
&\lesssim \sum_{E\in\mathcal{T}_h} \left(\|\mathbf{z}+\overline{\mathbf{K}}_E\nabla s^1\|_E + h|\mathbf{z}+\overline{\mathbf{K}}_E\nabla s^1|_{1,E}\right)\|\mathbf{q}\|_E \\
&\lesssim h(\|p\|_2+|\mathbf{z}|_1)\|\mathbf{q}\|, \qquad (4.19)
\end{aligned}
$$

using (2.64) and (4.18). A combination of (4.17) and (4.19) completes the proof. □

Remark 4.1 The analysis of Lemma 4.6 for the symmetric and nonsymmetric MFMFE methods is different due to the fact that accuracy of the interpolant Π deteriorates on general hexahedral grids, see (2.57).

In the analysis below, we utilize the following space-time norms. For any functional space S in Ω with a norm $\|\cdot\|_S$, let

$$
\begin{aligned}
\|\varphi\|_{L^2(S)} &= \left(\int_0^T \|\varphi(t)\|_S^2\,dt\right)^{1/2}, \\
\|\varphi\|_{L^\infty(S)} &= \operatorname{ess\,sup}_{t\in[0,T]}\|\varphi(t)\|_S.
\end{aligned}
$$

Theorem 4.1 *The solution* $(\mathbf{u}_h, p_h, \mathbf{z}_h)$ *of* (2.18)–(2.21) *with the symmetric quadrature rule satisfies*

$$
\begin{aligned}
&\|\mathbf{u}-\mathbf{u}_h\|_{L^\infty(H^1)} + \|p-p_h\|_{L^\infty(L^2)} + \|\mathbf{z}-\mathbf{z}_h\|_{L^2(L^2)} \\
&\lesssim h\left(\|\mathbf{u}\|_{L^\infty(H^2)} + \|\mathbf{u}_t\|_{L^2(H^2)} + \|p\|_{L^\infty(H^1)}\right. \\
&\qquad \left.+\|p_t\|_{L^2(H^1)} + \|\mathbf{z}\|_{L^2(H^1)}\right).
\end{aligned}
$$

The solution in the case of the nonsymmetric quadrature rule satisfies

$$
\begin{aligned}
&\|\mathbf{u}-\mathbf{u}_h\|_{L^\infty(H^1)} + \|p-p_h\|_{L^\infty(L^2)} + \|\Pi\mathbf{z}-\mathbf{z}_h\|_{L^2(L^2)} \\
&\lesssim h\left(\|\mathbf{u}\|_{L^\infty(H^2)} + \|\mathbf{u}_t\|_{L^2(H^2)} + \|p\|_{L^\infty(H^1)}\right. \\
&\qquad \left.+\|p_t\|_{L^2(H^1)} + \|p\|_{L^2(H^2)} + \|\mathbf{z}\|_{L^2(H^1)}\right).
\end{aligned}
$$

Proof Take $\mathbf{v} = (P_h\mathbf{u}-\mathbf{u}_h)_t$, $\mathbf{q} = \Pi\mathbf{z}-\mathbf{z}_h$, and $w = Q_hp - p_h$ in (4.1)–(4.3) and sum to obtain

$$
\begin{aligned}
&\frac{1}{2}a(P_h\mathbf{u}-\mathbf{u}_h, P_h\mathbf{u}-\mathbf{u}_h)_t + \frac{1}{2}(c_0(Q_hp-p_h), Q_hp-p_h)_t \\
&+\left(\mathbf{K}^{-1}(\Pi\mathbf{z}-\mathbf{z}_h), \Pi\mathbf{z}-\mathbf{z}_h\right)_Q \\
&= T_1(P_h\mathbf{u}-\mathbf{u}_h)_t + T_2(\Pi\mathbf{z}-\mathbf{z}_h) + T_3(Q_hp-p_h).
\end{aligned}
$$

Integrating in time from 0 to t and using the initial conditions (2.21) gives

$$
\begin{aligned}
&\frac{1}{2}\left(a(P_h\mathbf{u}-\mathbf{u}_h, P_h\mathbf{u}-\mathbf{u}_h) + (c_0(Q_hp-p_h), Q_hp-p_h)\right) \\
&\quad + \int_0^t \left(\mathbf{K}^{-1}(\Pi\mathbf{z}-\mathbf{z}_h), \Pi\mathbf{z}-\mathbf{z}_h\right)_Q d\tau \\
&= \int_0^t T_1\left((P_h\mathbf{u}-\mathbf{u}_h)_t\right)d\tau + \int_0^t T_2(\Pi\mathbf{z}-\mathbf{z}_h)\,d\tau \\
&\quad + \int_0^t T_3(Q_hp-p_h)\,d\tau. \qquad (4.20)
\end{aligned}
$$

The first term on the right above can be bounded by integrating by parts in time:

$$
\begin{aligned}
&\left|\int_0^t T_1\left((P_h\mathbf{u}-\mathbf{u}_h)_t\right)d\tau\right| \\
&= \left|-\alpha\int_0^t ((p-Q_hp)_t, \nabla\cdot(P_h\mathbf{u}-\mathbf{u}_h))\,d\tau\right. \\
&\quad \left.+\,\alpha(p-Q_hp, \nabla\cdot(P_h\mathbf{u}-\mathbf{u}_h))(t)\right| \\
&\le \frac{\alpha}{2}\int_0^t \|(p-Q_hp)_t\|^2\,d\tau + \frac{\alpha}{2}\int_0^t \|P_h\mathbf{u}-\mathbf{u}_h\|_1^2\,d\tau \\
&\quad + \frac{\alpha}{4\varepsilon}\|(p-Q_hp)(t)\|^2 + \alpha\varepsilon\|(P_h\mathbf{u}-\mathbf{u}_h)(t)\|_1^2, \qquad (4.21)
\end{aligned}
$$

where we have used (2.21) and the Young's inequality

$$
ab \le \varepsilon a^2 + \frac{1}{4\varepsilon}b^2.
$$

For the second term on the right in (4.20), using (4.7) or (4.8), we have

$$
\begin{aligned}
\left|\int_0^t T_2(\Pi\mathbf{z}-\mathbf{z}_h)\,d\tau\right| &\lesssim \frac{h^2}{4\varepsilon}\int_0^t \left(\|\mathbf{z}\|_1^2 + \sigma\|p\|_2^2\right)d\tau \\
&\quad + \varepsilon\int_0^t \|\Pi\mathbf{z}-\mathbf{z}_h\|^2\,d\tau, \qquad (4.22)
\end{aligned}
$$

where $\sigma = 0$ in the symmetric case and $\sigma = 1$ in the nonsymmetric case. The bound on the last term in (4.20) is

$$
\begin{aligned}
\left|\int_0^t T_3(Q_hp-p_h)\,d\tau\right| &\le \frac{\alpha}{2}\int_0^t \|(P_h\mathbf{u}-\mathbf{u})_t\|_1^2\,d\tau \\
&\quad + \frac{\alpha}{2}\int_0^t \|Q_hp-p_h\|^2\,d\tau. \qquad (4.23)
\end{aligned}
$$

Combining (4.20)–(4.23), taking ε small enough, and using (2.6), (2.17), the Gronwall inequality, (2.55), (2.59), and (2.60), we obtain

$$\begin{aligned}\|P_h\mathbf{u}-\mathbf{u}_h\|_{L^\infty(H^1)} &+ \|Q_hp-p_h\|_{L^\infty(L^2)}+\|\Pi\mathbf{z}-\mathbf{z}_h\|_{L^2(L^2)}\\ &\lesssim h\left(\|\mathbf{u}_t\|_{L^2(H^2)}+\|p\|_{L^\infty(H^1)}\right.\\ &+\|p_t\|_{L^2(H^1)}+\sigma\|p\|_{L^2(H^2)}\\ &+\left.\|\mathbf{z}\|_{L^2(H^1)}\right).\end{aligned}$$

An application of the triangle inequality and (2.21), (2.54), (2.59), and, in the case of the symmetric method, (2.56) and (2.58), completes the proof of the theorem. □

In the nonsymmetric case, using the approach in [47], we can also derive an estimate for the velocity error on element edges (faces). Consider the space-time extension of the face norm $\|\cdot\|_{\mathcal{F}_h}$ defined in (3.79):

$$\|\mathbf{q}\|_{L^2(\mathcal{F}_h)}=\left(\int_0^T\|\mathbf{q}(t)\|^2_{\mathcal{F}_h}\,dt\right)^{1/2}.$$

The proof of the result below follows from the argument of Lemma 3.14 and Theorem 3.2 in [47].

Theorem 4.2 *The velocity* $\mathbf{z}_h$ *of* (2.18)–(2.21) *with the nonsymmetric quadrature rule, on general quadrilaterals and hexahedra, satisfies*

$$\begin{aligned}\|\mathbf{z}-\mathbf{z}_h\|_{L^2(\mathcal{F}_h)}\lesssim h\left(\|\mathbf{u}\|_{L^\infty(H^2)}\|\mathbf{u}_t\|_{L^2(H^2)}+\|p\|_{L^\infty(H^1)}\right.\\ +\|p_t\|_{L^2(H^1)}+\|p\|_{L^2(H^2)}+\left.\|\mathbf{z}\|_{L^2(H^1)}\right).\end{aligned}$$

On general quadrilaterals with the nonsymmetric quadrature rule, the following error estimate holds by the interpolation estimate (2.56) and Theorem 4.1.

Theorem 4.3 *The velocity* $\mathbf{z}_h$ *of* (2.18)–(2.21) *with the nonsymmetric quadrature rule on general quadrilaterals satisfies*

$$\begin{aligned}\|\mathbf{z}-\mathbf{z}_h\|_{L^2(L^2)}\lesssim h\left(\|\mathbf{u}\|_{L^\infty(H^2)}+\|\mathbf{u}_t\|_{L^2(H^2)}+\|p\|_{L^\infty(H^1)}\right.\\ +\|p_t\|_{L^2(H^1)}+\|p\|_{L^2(H^2)}+\left.\|\mathbf{z}\|_{L^2(H^1)}\right).\end{aligned}$$

5 Convergence of the fully discrete poroelasticity scheme

We employ the backward Euler method for time discretization to obtain a fully discrete scheme. Let $0=t_0<t_1<\cdots<t_N=T$ be a partition of $[0,T]$. Let $\Delta t_n=t_{n+1}-t_n$, $n=0,\ldots,N-1$. We will use the notation $\varphi^n=\varphi(t_n)$. Let

$$\partial_t^{n+1}\varphi=\frac{\varphi^{n+1}-\varphi^n}{\Delta t_n}.$$

The fully discrete CG-MFMFE method for approximating (2.13)–(2.16) is: find $\mathbf{u}_h^{n+1}\in\mathbf{V}_h$, $\mathbf{z}_h^{n+1}\in\mathbf{Z}_h$, and $p_h^{n+1}\in W_h$, $n=0,\ldots,N-1$, satisfying

$$\begin{aligned}a\left(\mathbf{u}_h^{n+1},\mathbf{v}\right)-\alpha\left(p_h^{n+1},\nabla\cdot\mathbf{v}\right)&\\ =(\mathbf{f}^{n+1},\mathbf{v})+\langle\mathbf{t}_N,\mathbf{v}\rangle_{\Gamma_\sigma},\ \forall\,\mathbf{v}\in\mathbf{V}_h,&\quad(5.1)\\ \left(\mathbf{K}^{-1}\mathbf{z}_h^{n+1},\mathbf{q}\right)_Q-(p_h^{n+1},\nabla\cdot\mathbf{q})=0,\forall\mathbf{q}\in\mathbf{Z}_h,&\quad(5.2)\\ \left(c_0\partial_t^{n+1}p_h+\alpha\partial_t^{n+1}\nabla\cdot\mathbf{u}_h,w\right)+\left(\nabla\cdot\mathbf{z}_h^{n+1},w\right)&\\ =(s^{n+1},w),\forall\,w\in W_h,&\quad(5.3)\\ \mathbf{u}_h^0=P_h\mathbf{u}_0,\quad p_h^0=Q_hp_0.&\quad(5.4)\end{aligned}$$

We will use the following discrete space-time norms. For any functional space S in Ω with a norm $\|\cdot\|_S$, let

$$\begin{aligned}\|\varphi\|_{l^2(S)}&=\left(\sum_{n=0}^{N-1}\|\varphi^{n+1}\|_S^2\Delta t_n\right)^{1/2},\\ \|\varphi\|_{l^\infty(S)}&=\max_{0\le n\le N}\|\varphi^n\|_S.\end{aligned}$$

In the analysis below, we will use in several occasions that

$$\partial_t^{n+1}\varphi=\varphi_t^{n+1}+\frac{\Delta t_n}{2}\varphi_{tt}(\theta^n),\quad \theta^n\in[t_n,t_{n+1}].$$

Theorem 5.1 *The solution* $(\mathbf{u}_h,p_h,\mathbf{z}_h)$ *of* (5.1)–(5.4) *with the symmetric quadrature rule satisfies*

$$\begin{aligned}\|\mathbf{u}-\mathbf{u}_h\|_{l^\infty(H^1)}+\|p-p_h\|_{l^\infty(L^2)}+\|\mathbf{z}-\mathbf{z}_h\|_{l^2(L^2)}&\\ \lesssim(h+\Delta t)\left(\|\mathbf{u}\|_{l^\infty(H^2)}\right.&\\ +\|\mathbf{u}_t\|_{l^2(H^2)}+\|\mathbf{u}_{tt}\|_{L^\infty(H^1)}+\|p\|_{l^\infty(H^1)}&\\ +\left.\|p_t\|_{l^2(H^1)}+\|p_{tt}\|_{L^\infty(L^2)}+\|\mathbf{z}\|_{l^2(H^1)}\right).&\end{aligned}$$

The solution in the case of the nonsymmetric quadrature rule satisfies

$$\begin{aligned}\|\mathbf{u}-\mathbf{u}_h\|_{l^\infty(H^1)}+\|p-p_h\|_{l^\infty(L^2)}+\|\Pi\mathbf{z}-\mathbf{z}_h\|_{l^2(L^2)}&\\ \lesssim(h+\Delta t)\left(\|\mathbf{u}\|_{l^\infty(H^2)}\right.&\\ +\|\mathbf{u}_t\|_{l^2(H^2)}+\|\mathbf{u}_{tt}\|_{L^\infty(H^1)}+\|p\|_{l^\infty(H^1)}&\\ +\|p_t\|_{l^2(H^1)}+\|p_{tt}\|_{L^\infty(L^2)}+\|p\|_{l^2(H^2)}&\\ +\left.\|\mathbf{z}\|_{l^2(H^1)}\right).&\end{aligned}$$

Proof Subtracting (5.1)–(5.3) from (2.13)–(2.15) for each n from 0 to $N-1$, we obtain the error equations

$$\begin{aligned}a\left((P_h\mathbf{u}-\mathbf{u}_h)^{n+1},\mathbf{v}\right)-\alpha\left((Q_hp-p_h)^{n+1},\nabla\cdot\mathbf{v}\right)&\\ =\alpha\left((p-Q_hp)^{n+1},\nabla\cdot\mathbf{v}\right),\qquad\forall\,\mathbf{v}\in\mathbf{V}_h,&\quad(5.5)\end{aligned}$$

$$\left(\mathbf{K}^{-1}(\Pi\mathbf{z}-\mathbf{z}_h)^{n+1},\mathbf{q}\right)_Q-\left((Q_hp-p_h)^{n+1},\nabla\cdot\mathbf{q}\right)$$
$$=-(\mathbf{K}^{-1}\mathbf{z}^{n+1},\mathbf{q})+\left(\mathbf{K}^{-1}(\Pi\mathbf{z})^{n+1},\mathbf{q}\right)_Q,\ \forall\mathbf{q}\in\mathbf{Z}_h, \tag{5.6}$$

$$\left(c_0\partial_t^{n+1}(Q_hp-p_h)+\alpha\partial_t^{n+1}\nabla\cdot(P_h\mathbf{u}-\mathbf{u}_h),w\right)$$
$$+(\nabla\cdot(\Pi\mathbf{z}-\mathbf{z}_h)^{n+1},w)$$
$$=\left(\alpha\partial_t^{n+1}\nabla\cdot(P_h\mathbf{u}-\mathbf{u}),w\right)+(r^{n+1},w),\forall\, w\in W_h, \tag{5.7}$$

where

$$r^{n+1}\equiv-c_0\left(p_t^{n+1}-\partial_t^{n+1}p\right)-\alpha\left((\nabla\cdot\mathbf{u})_t^{n+1}-\partial_t^{n+1}\nabla\cdot\mathbf{u}\right). \tag{5.8}$$

Denote the right hand sides of (5.5)–(5.7) by $T_1^{n+1}(\mathbf{v})$, $T_2^{n+1}(\mathbf{q})$, and $T_3^{n+1}(w)$. Taking $\mathbf{v}=\partial_t^{n+1}(P_h\mathbf{u}-\mathbf{u}_h)$, $\mathbf{q}=(\Pi\mathbf{z}-\mathbf{z}_h)^{n+1}$, and $w=(Q_hp-p_h)^{n+1}$ in (5.5)–(5.7), summing, and using that for any ξ and for any inner product $(\cdot,\cdot)_*$

$$(\xi^{n+1},\xi^{n+1}-\xi^n)_*\geq\frac{1}{2}(\xi^{n+1},\xi^{n+1})_*-\frac{1}{2}(\xi^n,\xi^n)_*,$$

we obtain

$$\frac{1}{2\Delta t_n}\left(\|(P_h\mathbf{u}-\mathbf{u}_h)^{n+1}\|_a^2-\|(P_h\mathbf{u}-\mathbf{u}_h)^n\|_a^2\right)$$
$$+\frac{c_0}{2\Delta t_n}\left(\|(Q_hp-p_h)^{n+1}\|^2-\|(Q_hp-p_h)^n\|^2\right)$$
$$+\left(\mathbf{K}^{-1}(\Pi\mathbf{z}-\mathbf{z}_h)^{n+1},(\Pi\mathbf{z}-\mathbf{z}_h)^{n+1}\right)_Q$$
$$\leq T_1^{n+1}\left(\partial_t^{n+1}(P_h\mathbf{u}-\mathbf{u}_h)\right)+T_2^{n+1}\left((\Pi\mathbf{z}-\mathbf{z}_h)^{n+1}\right)$$
$$+T_3^{n+1}\left((Q_hp-p_h)^{n+1}\right), \tag{5.9}$$

where $\|\mathbf{v}\|_a^2=a(\mathbf{v},\mathbf{v})$. Multiplying by Δt_n and summing for $n=0$ to $N-1$ gives

$$\frac{1}{2}\|(P_h\mathbf{u}-\mathbf{u}_h)^N\|_a^2+\frac{c_0}{2}\|(Q_hp-p_h)^N\|^2$$
$$+\sum_{n=0}^{N-1}\Delta t_n\|\mathbf{K}^{-1/2}(\Pi\mathbf{z}-\mathbf{z}_h)^{n+1}\|_Q^2$$
$$\leq\sum_{n=0}^{N-1}T_1^{n+1}\left(\partial_t^{n+1}(P_h\mathbf{u}-\mathbf{u}_h)\right)\Delta t_n$$
$$+\sum_{n=0}^{N-1}T_2^{n+1}\left((\Pi\mathbf{z}-\mathbf{z}_h)^{n+1}\right)\Delta t_n$$
$$+\sum_{n=0}^{N-1}T_3^{n+1}\left((Q_hp-p_h)^{n+1}\right)\Delta t_n, \tag{5.10}$$

where we have used the initial conditions (5.4). The first term on the right above can be bounded using discrete integration by parts in time

$$\sum_{n=0}^{N-1}\xi^{n+1}(\eta^{n+1}-\eta^n)=\xi^N\eta^N-\sum_{n=0}^{N-1}(\xi^{n+1}-\xi^n)\eta^n-\xi^0\eta^0.$$

We have, using (5.4),

$$\sum_{n=0}^{N-1}T_1^{n+1}\left(\partial_t^{n+1}(P_h\mathbf{u}-\mathbf{u}_h)\right)\Delta t_n$$
$$=\alpha\sum_{n=0}^{N-1}\left((p-Q_hp)^{n+1},\nabla\cdot\partial_t^{n+1}(P_h\mathbf{u}-\mathbf{u}_h)\right)\Delta t_n$$
$$=\alpha\left((p-Q_hp)^N,\nabla\cdot(P_h\mathbf{u}-\mathbf{u}_h)^N\right)$$
$$-\alpha\sum_{n=0}^{N-1}\left(\partial_t^{n+1}(p-Q_hp),\nabla\cdot(P_h\mathbf{u}-\mathbf{u}_h)^n\right)\Delta t_n$$
$$\leq\frac{\alpha}{4\varepsilon}\|(p-Q_hp)^N\|^2+\alpha\epsilon\|(P_h\mathbf{u}-\mathbf{u}_h)^N\|_1^2$$
$$+\frac{\alpha}{2}\sum_{n=0}^{N-1}\left(\|(p-Q_hp)_t^{n+1}\|+\frac{\Delta t_n}{2}\|p_{tt}\|_{L^\infty(L^2)}\right)^2\Delta t_n$$
$$+\frac{\alpha}{2}\sum_{n=0}^{N-1}\|(P_h\mathbf{u}-\mathbf{u}_h)^n\|_1^2\Delta t_n. \tag{5.11}$$

For the second term on the right in (5.10), using Lemma 4.2, we have

$$\sum_{n=0}^{N-1}T_2^{n+1}\left((\Pi\mathbf{z}-\mathbf{z}_h)^{n+1}\right)\Delta t_n$$
$$\lesssim\frac{h^2}{4\varepsilon}\left(\|\mathbf{z}\|_{l^2(H^1)}^2+\sigma\|p\|_{l^2(H^2)}\right)$$
$$+\epsilon\sum_{n=0}^{N-1}\|(\Pi\mathbf{z}-\mathbf{z}_h)^{n+1}\|^2\Delta t_n, \tag{5.12}$$

where $\sigma=0$ in the symmetric case and $\sigma=1$ in the non-symmetric case. The last term on the right in (5.10) can be bounded as

$$\sum_{n=0}^{N-1}T_3^{n+1}((Q_hp-p_h)^{n+1})\Delta t_n\leq\frac{\alpha}{4\varepsilon}\sum_{n=0}^{N-1}\|\partial_t^{n+1}\nabla\cdot(P_h\mathbf{u}-\mathbf{u})\|^2\Delta t_n$$
$$+\frac{1}{4\varepsilon}\sum_{n=0}^{N-1}\|r^{n+1}\|^2\Delta t_n+(\alpha+1)\varepsilon\sum_{n=0}^{N-1}\|(Q_hp-p_h)^{n+1}\|^2\Delta t_n$$
$$\leq\frac{\alpha}{4\varepsilon}\sum_{n=0}^{N-1}\left(\|\nabla\cdot(P_h\mathbf{u}-\mathbf{u})_t^{n+1}\|+\frac{\Delta t_n}{2}\|\nabla\cdot\mathbf{u}_{tt}\|_{L^\infty(L^2)}\right)^2\Delta t_n$$
$$+\frac{1}{4\varepsilon}\sum_{n=0}^{N-1}\left(c_0\frac{\Delta t_n}{2}\|p_{tt}\|_{L^\infty(L^2)}+\alpha\frac{\Delta t_n}{2}\|\nabla\cdot\mathbf{u}_{tt}\|_{L^\infty(L^2)}\right)^2\Delta t_n$$
$$+(\alpha+1)\varepsilon\sum_{n=0}^{N-1}\|(Q_hp-p_h)^{n+1}\|^2\Delta t_n. \tag{5.13}$$

A combination of (5.10)–(5.13), taking ε small enough, and using (2.6), (2.17), (5.4), the discrete Gronwall inequality, and the approximation properties (2.55), (2.59), and (2.60), gives

$$\begin{aligned}\|P_h\mathbf{u}-\mathbf{u}_h\|_{l^\infty(H^1)}+\|Q_hp-p_h\|_{l^\infty(L^2)}+\|\Pi\mathbf{z}-\mathbf{z}_h\|_{l^2(L^2)}\\ \lesssim (h+\Delta t)\left(\|\mathbf{u}_t\|_{l^2(H^2)}+\|\mathbf{u}_{tt}\|_{L^\infty(H^1)}\right.\\ +\|p\|_{l^\infty(H^1)}+\|p_t\|_{l^2(H^1)}+\|p_{tt}\|_{L^\infty(L^2)}\\ \left.+\sigma\|p\|_{l^2(H^2)}+\|\mathbf{z}\|_{l^2(H^1)}\right).\end{aligned} \tag{5.14}$$

The statement of the theorem follows from the triangle inequality and the application of (2.54), (2.59), (5.4), and, in the case of the symmetric method, (2.56) and (2.58). □

In the nonsymmetric case, similar to the semidiscrete case, we can also derive an estimate for the velocity error on element edges (faces). The proof of the result below follows from the argument of Lemma 3.14 and Theorem 3.2 in [47].

Theorem 5.2 *The velocity* $\mathbf{z}_h$ *of* (5.1)–(5.4) *with the nonsymmetric quadrature rule satisfies*

$$\begin{aligned}\|\mathbf{z}-\mathbf{z}_h\|_{l^2(\mathcal{F}_h)}\lesssim (h+\Delta t)\left(\|\mathbf{u}\|_{l^\infty(H^2)}+\|\mathbf{u}_t\|_{l^2(H^2)}\right.\\ +\|\mathbf{u}_{tt}\|_{L^\infty(H^1)}+\|p\|_{l^\infty(H^1)}\\ +\|p_t\|_{l^2(H^1)}+\|p_{tt}\|_{L^\infty(L^2)}\\ \left.+\|p\|_{l^2(H^2)}+\|\mathbf{z}\|_{l^2(H^1)}\right).\end{aligned}$$

On general quadrilaterals with the nonsymmetric quadrature rule, similarly to Theorem 4.3 in the semidiscrete case, we have the following result.

Theorem 5.3 *The velocity* $\mathbf{z}_h$ *of* (5.1)–(5.4) *with the nonsymmetric quadrature rule on general quadrilaterals satisfies*

$$\begin{aligned}\|\mathbf{z}-\mathbf{z}_h\|_{l^2(L^2)}\lesssim (h+\Delta t)\left(\|\mathbf{u}\|_{l^\infty(H^2)}+\|\mathbf{u}_t\|_{l^2(H^2)}\right.\\ +\|\mathbf{u}_{tt}\|_{L^\infty(H^1)}+\|p\|_{l^\infty(H^1)}\\ +\|p_t\|_{l^2(H^1)}+\|p_{tt}\|_{L^\infty(L^2)}\\ \left.+\|p\|_{l^2(H^2)}+\|\mathbf{z}\|_{l^2(H^1)}\right).\end{aligned}$$

6 Computational experiments

In this section, we present several numerical experiments in two dimensions designed to test the theoretical convergence rates. We also illustrate the behavior of the method on a problem with curved boundaries motivated by the cantilever bracket problem.

6.1 Convergence tests

We first perform numerical convergence tests for the spatial discretization of the problem (2.1)–(2.3) with given analytical solutions

$$\mathbf{u}=\begin{pmatrix}\sin(\pi t)x(1-x)y(1-y)\\ \sin(\pi t)x(1-x)y(1-y)\end{pmatrix}\quad\text{and}$$
$$p=t\sin(2\pi x)\sin(2\pi y).$$

The parameters in the equations are chosen to be $\alpha=1$, $\nu=0.2$, $E=1$, $c_0=0.1$, and a full permeability tensor

$$\mathbf{K}=\begin{pmatrix}3&1\\1&2\end{pmatrix}.$$

The boundary conditions are of Dirichlet type for both the displacement and the pressure. The source terms in the equations are specified accordingly. We consider a sequence of smooth and randomly perturbed quadrilateral meshes, as well as Kershaw meshes [45] and triangular meshes, see Fig. 2.

The grid points in the quadrilateral meshes are defined by mapping the grid points in a sequence of refined uniform rectangular meshes. The smooth mapping is given by:

$$\begin{aligned}x&=\hat{x}+0.06\sin(2\pi\hat{x})\sin(2\pi\hat{y}),\\ y&=\hat{y}-0.05\sin(2\pi\hat{x})\sin(2\pi\hat{y}),\end{aligned}$$

where $(\hat{x},\hat{y})$ is a grid point in the uniform mesh and (x,y) is the corresponding grid point in the quadrilateral mesh. Similarly, the interior grid points in the randomly perturbed quadrilateral meshes are given by the mapping

$$x=\hat{x}+h\eta_x,\qquad y=\hat{y}+h\eta_y,$$

where h is the discretization parameter of the current level of refinement and η_x and η_y are random numbers between -0.25 and 0.25. Figure 2 shows the smooth and randomly perturbed quadrilateral meshes as well as the triangular mesh on a level of 20 by 20, and Kershaw mesh on a level of 16 by 16.

Both the symmetric and the nonsymmetric methods for flow are tested. The time step size is $\Delta t=10^{-2}$ and the final simulation time is $T=0.5$.

Table 1 shows the convergence on the smooth quadrilateral meshes. As the theory predicts both the symmetric and the nonsymmetric MFMFE method for flow give first-order convergence with respect to $\|\mathbf{u}-\mathbf{u}_h\|_{L^\infty(H^1)}$, $\|\mathbf{z}-\mathbf{z}_h\|_{L^2(L^2)}$ and $\|p-p_h\|_{L^\infty(L^2)}$.

Table 2 shows the convergence on the randomly perturbed quadrilateral meshes. Since these elements are not h^2-parallelograms, the convergence order of the symmetric MFMFE method for the flow deteriorates and it affects the convergence order for displacements. On the other hands, as the theory predicts, the nonsymmetric MFMFE method has

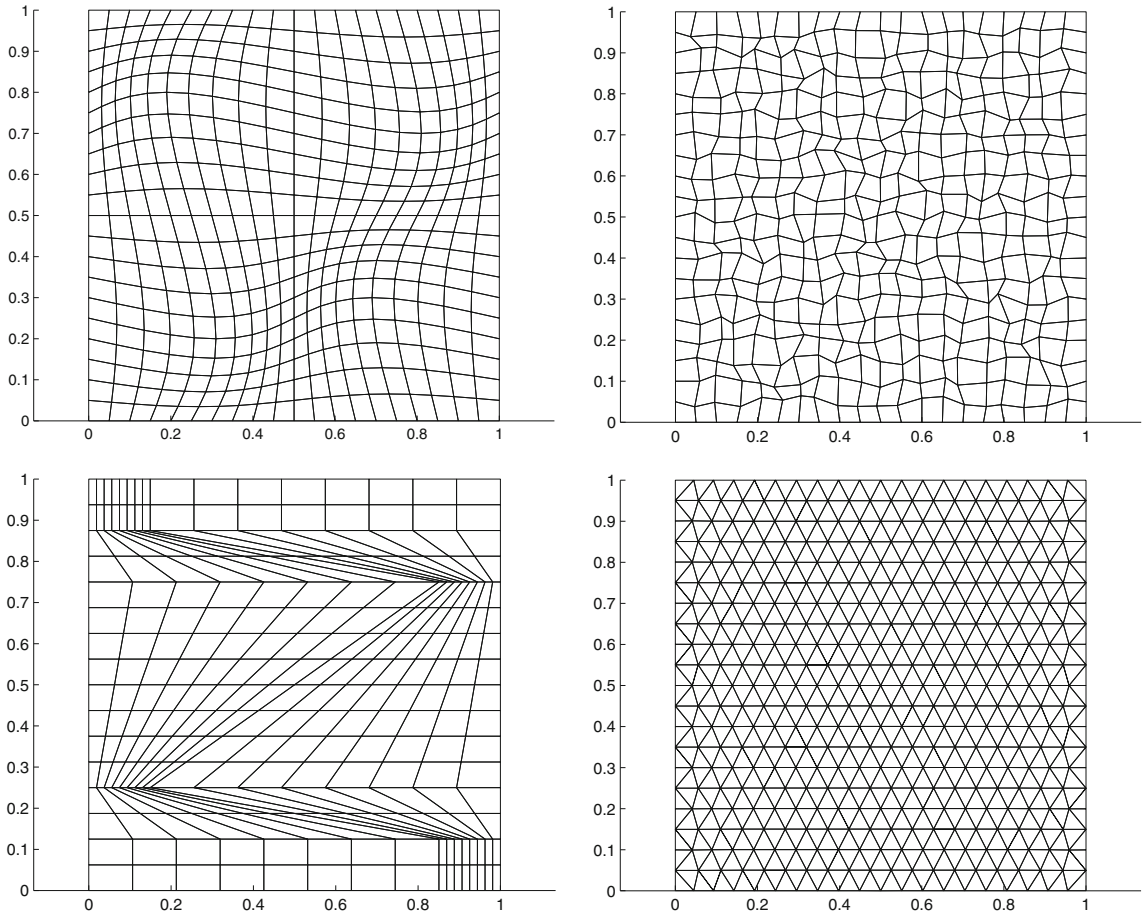

Fig. 2 Smooth quadrilateral mesh (*top left*), randomly perturbed quadrilateral mesh (*top right*), Kershaw mesh (*bottom left*), and triangular mesh (*bottom right*)

first-order convergence for the flow and displacement also has first-order convergence.

On the Kershaw meshes in Table 3, both the symmetric and the nonsymmetric MFMFE methods exhibit first-order convergence for the flow and the displacement. Even though the coarse grid is very rough, the sequence of meshes is obtained via a uniform refinement. This results in h^2-perturbed grids, which explains the convergence of both methods. Nevertheless, this example indicates that the methods can handle well irregularly shaped elements.

Table 1 Convergence on smooth quadrilaterals

h	$\|\mathbf{u}-\mathbf{u}_h\|_{l^\infty(H^1)}$	Rate	$\|p-p_h\|_{l^\infty(L^2)}$	Rate	$\|\mathbf{z}-\mathbf{z}_h\|_{l^2(L^2)}$	Rate
Symmetric MFMFE method for flow						
1/10	4.23e-02	–	6.76e-02	–	4.62e-01	–
1/20	1.53e-02	1.47	3.38e-02	1.00	2.00e-01	1.21
1/40	6.44e-03	1.25	1.69e-02	1.00	9.53e-02	1.07
1/80	3.04e-03	1.08	8.44e-03	1.00	4.70e-02	1.02
1/160	1.50e-03	1.02	4.22e-03	1.00	2.34e-02	1.01
Nonsymmetric MFMFE method for flow						
1/10	4.16e-02	–	6.73e-02	–	4.65e-01	–
1/20	1.50e-02	1.47	3.37e-02	1.00	2.02e-01	1.20
1/40	6.40e-03	1.23	1.69e-02	1.00	9.65e-02	1.07
1/80	3.04e-03	1.07	8.44e-03	1.00	4.77e-02	1.02
1/160	1.50e-03	1.02	4.22e-03	1.00	2.38e-02	1.00

Table 2 Convergence on randomly perturbed quadrilaterals

h	$\|\mathbf{u}-\mathbf{u}_h\|_{l^\infty(H^1)}$	Rate	$\|p-p_h\|_{l^\infty(L^2)}$	Rate	$\|\mathbf{z}-\mathbf{z}_h\|_{l^2(L^2)}$	Rate
Symmetric MFMFE method for flow						
1/10	4.28e-02	–	6.76e-02	–	4.84e-01	–
1/20	1.68e-02	1.35	3.40e-02	0.99	2.33e-01	1.05
1/40	7.90e-03	1.09	1.71e-02	0.99	1.51e-01	0.63
1/80	4.31e-03	0.87	8.80e-03	0.96	1.25e-01	0.27
1/160	3.00e-03	0.52	4.99e-03	0.82	1.23e-01	0.02
Nonsymmetric MFMFE method for flow						
1/10	4.14e-02	–	6.73e-02	–	4.80e-01	–
1/20	1.57e-02	1.40	3.37e-02	1.00	2.09e-01	1.20
1/40	7.03e-03	1.16	1.68e-02	1.00	1.00e-01	1.06
1/80	3.41e-03	1.04	8.40e-03	1.00	4.96e-02	1.01
1/160	1.71e-03	1.00	4.21e-03	1.00	2.48e-02	1.00

Table 3 Convergence on Kershaw mesh

h	$\|\mathbf{u}-\mathbf{u}_h\|_{l^\infty(H^1)}$	Rate	$\|p-p_h\|_{l^\infty(L^2)}$	Rate	$\|\mathbf{z}-\mathbf{z}_h\|_{l^2(L^2)}$	Rate
Symmetric MFMFE method for flow						
1/8	1.65e-01	–	1.69e-01	–	2.03e+00	–
1/16	8.44e-02	0.97	8.53e-02	0.99	1.05e+00	0.95
1/32	4.16e-02	1.02	4.02e-02	1.09	4.49e-01	1.23
1/64	1.92e-02	1.12	1.91e-02	1.07	1.71e-01	1.39
Nonsymmetric MFMFE method for flow						
1/8	1.49e-01	–	1.52e-01	–	1.45e+00	–
1/16	8.10e-02	0.88	8.20e-02	0.89	7.78e-01	0.90
1/32	4.07e-02	0.99	3.94e-02	1.06	3.24e-01	1.26
1/64	1.91e-02	1.09	1.90e-02	1.05	1.37e-01	1.24

Table 4 Convergence on triangles

h	$\|\mathbf{u}-\mathbf{u}_h\|_{l^\infty(H^1)}$	Rate	$\|p-p_h\|_{l^\infty(L^2)}$	Rate	$\|\mathbf{z}-\mathbf{z}_h\|_{l^2(L^2)}$	Rate
1/10	3.58e-02	–	5.08e-02	–	3.40e-01	–
1/20	1.50e-02	1.25	2.49e-02	1.03	1.35e-01	1.33
1/40	7.08e-03	1.08	1.24e-02	1.01	6.23e-02	1.12
1/80	3.45e-03	1.04	6.16e-03	1.01	3.03e-02	1.04
1/160	1.72e-03	1.00	3.07e-03	1.00	1.51e-02	1.00

Table 5 Convergence in time on a 160×160 triangular mesh

Δt	$\|\mathbf{u}-\mathbf{u}_h\|_{l^\infty(H^1)}$	Rate	$\|p-p_h\|_{l^\infty(L^2)}$	Rate	$\|\mathbf{z}-\mathbf{z}_h\|_{l^2(L^2)}$	Rate
1/8	6.51e-05	–	1.42e-05	–	7.58e-05	–
1/16	2.84e-05	1.20	6.32e-06	1.17	2.59e-05	1.55
1/32	1.30e-05	1.13	2.92e-06	1.11	9.82e-06	1.40
1/64	6.17e-06	1.08	1.40e-06	1.06	4.15e-06	1.24
1/128	3.02e-06	1.03	6.83e-07	1.04	1.89e-06	1.13

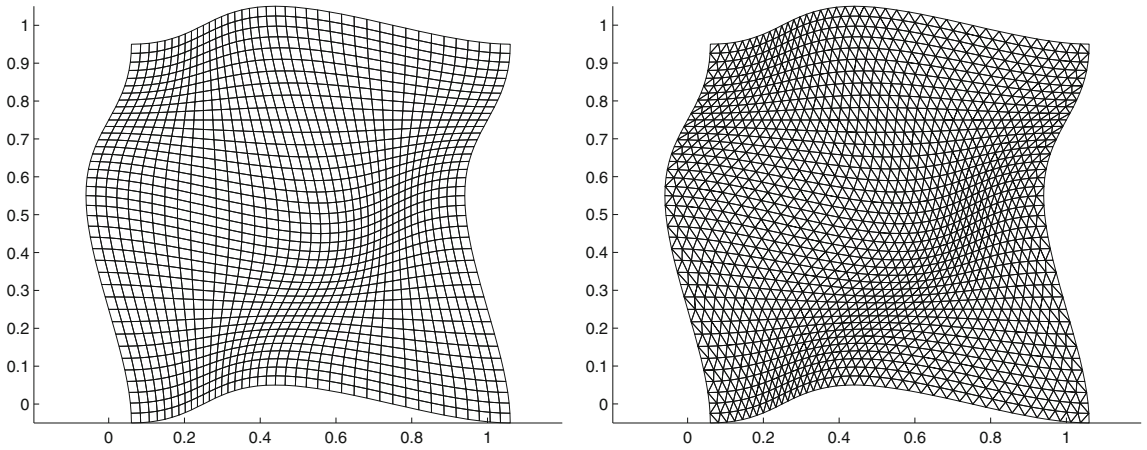

Fig. 3 Quadrilateral (*left*) and triangular mesh (*right*) for the cantilever bracket problem

On triangular meshes in Table 4, both the symmetric and nonsymmetric methods are the same since the Jacobian matrix is constant. As the theory indicates, we observe first-order convergence for the displacements, velocity, and pressure.

In the next example, we perform convergence study with respect to the discretization in time by fixing the spatial mesh. The exact solutions are chosen as

$$\mathbf{u} = \begin{pmatrix} t^{12}x(1-x)y(1-y) \\ t^{12}x(1-x)y(1-y) \end{pmatrix} \quad \text{and} \quad p = t^{12}x(1-x)y(1-y).$$

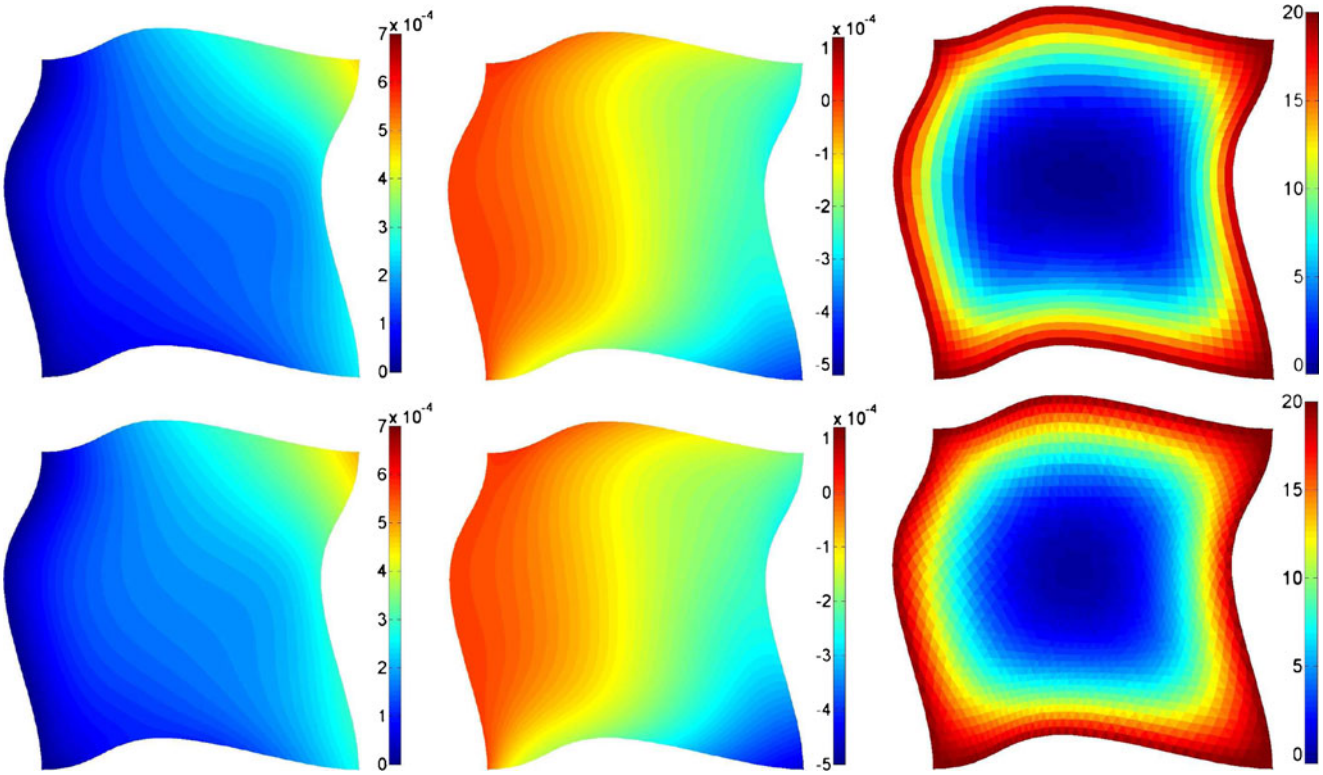

Fig. 4 Displacements in x direction (*left*) and y direction (*middle*), and pressure (*right*) on quadrilateral (*top row*) and triangular meshes (*bottom row*) for the cantilever bracket problem at time $t = 10$

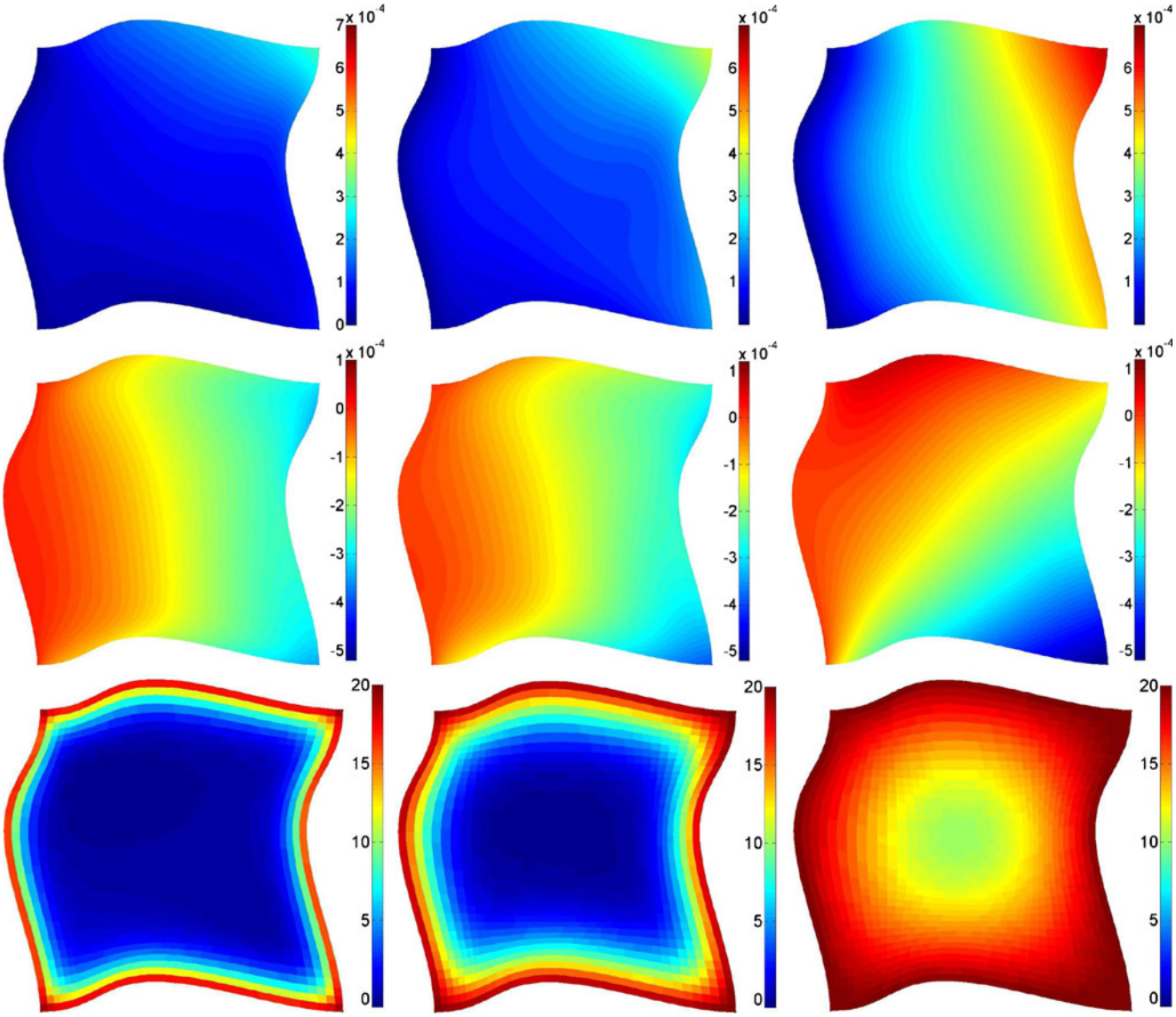

Fig. 5 Transients of displacement in x direction (*top row*) and y direction (*middle row*), and pressure (*bottom row*) at $t = 2, 6, 50$ for the cantilever bracket problem on the quadrilateral mesh

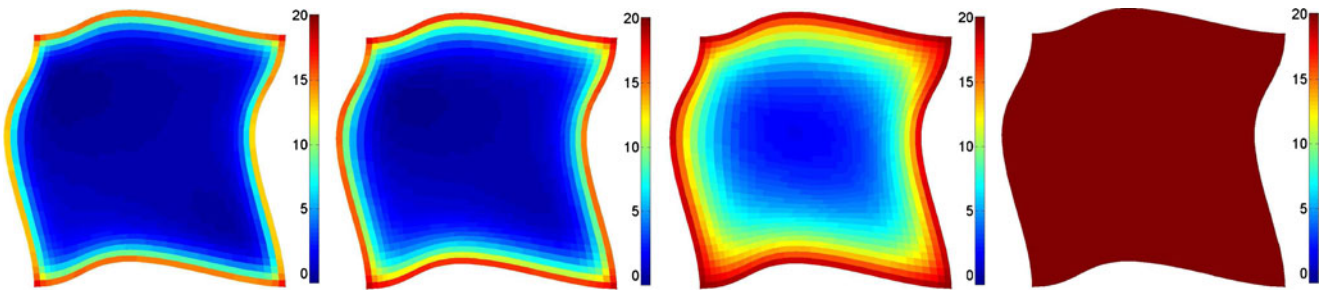

Fig. 6 The effect of the displacement to the flow: pressure at $t = 1$ for $\alpha = 1, 0.7, 0.3, 0$

The parameters in this example are $\alpha = 10$, $\nu = 0.2$, $E = 1$, $c_0 = 100$, and the permeability tensor is as in the previous example. The boundary conditions are of Dirichlet type for both the displacement and the pressure. The final time is $T = 0.5$. We run a sequence of simulations with refined time steps on a fixed 160×160 triangular spatial mesh. Table 5 indicates first-order convergence in time as the theory predicts.

6.2 An example with irregular geometry

Here, we illustrate the behavior of the method (2.18)–(2.21) for the poroelasticity system on a domain with curved boundaries using both quadrilateral and triangular meshes as shown in Fig. 3. The elasticity boundary conditions are motivated by the cantilever bracket problem. This problem was studied in [27, 35] for a fluid saturated bracket using the system of poroelasticity (2.1)–(2.3). The elasticity boundary conditions are

$$\begin{aligned} \mathbf{u} &= \mathbf{0} && \text{on } \Gamma_1, \\ \boldsymbol{\sigma}\mathbf{n} &= \mathbf{0} && \text{on } \Gamma_2 \cup \Gamma_3, \\ \boldsymbol{\sigma}\mathbf{n} &= (0,-1)^T && \text{on } \Gamma_4, \end{aligned}$$

where Γ_1 and Γ_2 are the left and right boundaries of Ω, and Γ_3 and Γ_4 are the bottom and top boundaries of Ω, respectively. The flow boundary condition is of Dirichlet type:

$$p = 20 \qquad \text{on } \partial\Omega.$$

The physical properties in (2.1)–(2.4) are given as $\nu = 0.4$, $E = 10^4$, $\mathbf{f} = \mathbf{0}$, $c_0 = 10^{-5}$, and $\mathbf{K} = 10^{-7}$. The source terms are $\mathbf{f} = \mathbf{0}$, $s = 0$, and the coupling parameter is $\alpha = 1$. The time step size is $\Delta t = 1$ in all subsequent numerical examples. The symmetric MFMFE method is applied for the flow discretization.

Figure 4 shows the displacement and pressure on quadrilateral and triangular meshes at time $t = 10$. The numerical solutions on the two different meshes agree well. The x displacement increases along the x direction and the y displacement decreases along the y direction due to the traction boundary condition at the top boundary and zero displacement at the left boundary. Although the pressure is constant on the boundary and the permeability is homogeneous, the interior pressure is much lower than the boundary pressure due to the coupling effect.

Figure 5 shows the transients of the displacements and the pressure on the quadrilateral mesh. When the solution reaches steady state at $t = 50$, the x displacement has maximum at the upper right corner while the y displacement has minimum at the lower right corner. The pressure initially exhibits a sharp boundary layer, which is smoothed out over time with the pressure gradually increasing in the interior. Still, at steady state, the pressure is lower in the interior than on the boundary.

To study the poroelasticity coupling effect on the pressure, we take $c_0 = 0$ and gradually vary $\alpha = 1$ to $\alpha = 0$. Figure 6 shows pressure profiles on the quadrilateral mesh at $t = 1$ with different α. As α decreases, the interior pressure becomes closer to the boundary pressure. When $\alpha = 0$, the elasticity and flow are decoupled and the pressure is constant on the whole domain due to the homogeneous permeability field.

7 Conclusions

The poroelasticity problem is discretized by the multipoint flux mixed finite element for flow and the continuous piecewise linear Galerkin finite element method for elasticity. A priori error analysis is carried out for the displacement, pressure, and velocity. A series of numerical experiments on quadrilateral and simplicial meshes are conducted to verify the theoretical convergence rates. The transient and coupling effects are studied on a curved domain for a problem motivated by the cantilever bracket problem.

Acknowledgments Mary Wheeler is partially supported by the DOE grant DE-FGO2-04ER25617. Guangri Xue was supported by award no. KUS-F1-032-04 by King Abdullah University of Science and Technology (KAUST) during his work at UT-Austin 2008-2011. Ivan Yotov is partially supported by the DOE grant DE-FG02-04ER25618, the NSF grant DMS 1115856, and the J. Tinsley Oden Faculty Fellowship, ICES, The University of Texas at Austin.

References

1. Aavastsmark, I., Eigestad, G.T., Klausen, R.A., Wheeler, M.F., Yotov, I.: Convergence of a symmetric MPFA method on quadrilateral grids. Comput. Geosci. **11**, 333–345 (2007)
2. Aavatsmark, I.: An introduction to multipoint flux approximations for quadrilateral grids. Comput. Geosci. **6**, 405–432 (2002)
3. Aavatsmark, I., Barkve, T., Boe, O., Mannseth, T.: Discretization on unstructured grids for inhomogeneous, anisotropic media, part II: discussion and numerical results. SIAM J. Sci. Comput. **19**, 1717–1736 (1998)
4. Arnold, D.N., Boffi, D., Falk, R.S.: Approximation by quadrilateral finite elements. Math. Comp. **71**, 909–922 (2002)
5. Arnold, D.N., Boffi, D., Falk, R.S.: Quadrilateral $H(\mathrm{div})$ finite elements. SIAM J. Numer. Anal. **42**, 2429–2451 (2005). (electronic)
6. Biot, M.A.: General theory of three-dimensional consolidation. J. Appl. Phys. **12**, 155–164 (1941)
7. Brenner, S.C., Scott, L.R.: The Mathematical Theory of Finite Element Methods, Texts in Applied Mathematics. Springer-Verlag (2007)
8. Brezzi, F., Douglas, J., Duran, R., Fortin, M.: Mixed finite elements for second order elliptic problems in three variables. Numer. Math. **51**, 237–250 (1987)

9. Brezzi, F., Douglas, J., Marini, L.D.: Two families of mixed finite elements for second order elliptic problems. Numer. Math. **47**, 217–235 (1985)
10. Brezzi, F., Fortin, M.: Mixed and hybrid finite element methods. Spring-Verlag, New York (1991)
11. Chin, L.Y., Raghavan, R., Thomas, L.: Iterative coupled analysis of geomechanics and fluid flow for rock compaction in reservoir simulation. Oil Gas Sci. Tech. **57**, 485–497 (2002)
12. Ciarlet, P.G.: The Finite Element Method for Elliptic Problems. Studies of Mathematics Applied, vol. 4. North-Holland, Amsterdam, 1978; reprinted, SIAM, Philadelphia (2002)
13. Edwards, M.G.: Unstructured control-volume distributed, full-tensor finite-volume schemes with flow based grids. Comput. Geosci. **6**, 433–452 (2002)
14. Edwards, M.G., Rogers, C.F.: Finite volume discretization with imposed flux continuity for the general tensor pressure equation. Comput. Geosci. **2**, 259–290 (1998)
15. Ewing, R.E., Iliev, O.P., Lazarov, R.D., Naumovich, A.: On convergence of certain finite volume difference discretizations for 1D poroelasticity interface problems. Numer. Methods Partial Differ. Equ. **23**, 652–671 (2007)
16. Falk, R.S., Gatto, P., Monk, P.: Hexahedral H(div) and H(curl) finite elements. Math. Mod. Numer. Anal. **45**(1), 115–143 (2011)
17. Gai, X.: A Coupled Geomechanics and Reservoir Flow Model on Parallel Computers. PhD thesis, University of Texas at Austin, Texas (2004)
18. Gai, X., Dean, R., Wheeler, M.F., Liu, R.: Coupled geomechanical and reservoir modeling on parallel computers. In: Proceedings of SPE Reservoir Symposium. SPE, Houston. SPE 79700 (2003)
19. Gaspar, F.J., Lisbona, F.J., Vabishchevich, P.N.: A finite difference analysis of Biot's consolidation model. Appl. Numer. Math. **44**, 487–506 (2003)
20. Girault, V., Pencheva, G., Wheeler, M.F., Wildey, T.M.: Domain decomposition for poroelasticity and elasticity with DG jumps and mortars. Math. Model. Meth. Appl. Sci. **21**, 169–213 (2011)
21. Ingram, R., Wheeler, M.F., Yotov, I.: A multipoint flux mixed finite element method on hexahedra. SIAM J. Numer. Anal. **48**, 1281–1312 (2010)
22. Klausen, R.A., Radu, F.A., Eigestad, G.T.: Convergence of MPFA on triangulations and for Richards' equation. Int. J. Numer. Meth. Fluids **58**, 1327–1351 (2008)
23. Klausen, R.A., Winther, R.: Convergence of multipoint flux approximations on quadrilateral grids. Numer. Methods Partial Differ. Equ. **22**, 1438–1454 (2006)
24. Klausen, R.A., Winther, R.: Robust convergence of multi point flux approximation on rough grids. Numer. Math. **104**, 317–337 (2006)
25. Korsawe, J., Starke, G.: A least-squares mixed finite element method for Biot's consolidation problem in porous media. SIAM J. Numer. Anal. **43**, 318–339 (2005). (electronic)
26. Korsawe, J., Starke, G., Wang, W., Kolditz, O.: Finite element analysis of poro-elastic consolidation in porous media: Standard and mixed approaches. Comput. Methods Appl. Mech. Eng. **195**, 1096–1115 (2006)
27. Liu, R.: Discontinuous Galerkin Finite Element Solution for Poromechanics. PhD thesis, The University of Texas at Austin (2004)
28. Liu, R., Wheeler, M.F., Dawson, C., Dean, R.: On a coupled discontinuous/continuous Galerkin framework and an adaptive penalty scheme for poroelasticity problems. Comput. Meth. Appl. Mech. Eng. **198**, 3499–3510 (2009)
29. Matthies, G.: Mapped finite elements on hexahedra. necessary and sufficient conditions for optimal interpolation errors. Numer. Algorithm. **27**, 317–327 (2001)
30. Murad, M.A., Loula, A.F.D.: Improved accuracy in finite element analysis of Biot's consolidation problem. Comput. Methods Appl. Mech. Engrg. **95**, 359–382 (1992)
31. Murad, M.A., Loula, A.F.D.: On stability and convergence of finite element approximations of Biot's consolidation problem. Int. J. Numer. Methods Eng. **37**, 645–667 (1994)
32. Murad, M.A., Thomée, V., Loula, A.F.D.: Asymptotic behavior of semidiscrete finite-element approximations of Biot's consolidation problem. SIAM J. Numer. Anal. **33**, 1065–1083 (1996)
33. Naff, R., Russell, T., Wilson, J.D.: Shape functions for velocity interpolation in general hexahedral cells. Comp. Geosci. **6**, 285–314 (2002)
34. Nedelec, J.C.: Mixed finite elements in r^3. Numer. Math. **35**, 315–341 (1980)
35. Phillips, P.J.: Finite Element Methods in Linear Poroelasticity: Theoretical and Computational Results. PhD thesis, University of Texas at Austin (2005)
36. Phillips, P.J., Wheeler, M.F.: A coupling of mixed and continuous Galerkin finite element methods for poroelasticity I: the continuous in time case. Comput. Geosci. **11**, 131–144 (2007)
37. Phillips, P.J., Wheeler, M.F.: A coupling of mixed and continuous Galerkin finite element methods for poroelasticity II: the discrete in time case. Comput. Geosci. **11**, 145–158 (2007)
38. Phillips, P.J., Wheeler, M.F.: A coupling of mixed and discontinuous Galerkin finite-element methods for poroelasticity. Comput. Geosci. **12**, 417–435 (2008)
39. Raviart, P.A., Thomas, J.: A mixed finite element method for 2-nd order elliptic problems. In: Galligani, I., Magenes, E. (eds.) Mathematical Aspects of the Finite Elements Method, Lectures Notes in Math, vol. 606, pp. 292–315. Springer, Berlin (1977)
40. Sboui, A., Jaffre, J., Roberts, J.: A composite mixed finite elements for hexahedral grids. SIAM J. Sci. Comput. **31**, 2623–2645 (2009)
41. Settari, A., Mourits, F.: Coupling of geomechanics and reservoir simulation models. In: Siriwardane, Zaman (eds.) Computer Methods and Advances in Geomechanics, pp. 2151–2158. Balkema Rotterdam (1994)
42. Showalter, R.: Diffusion in poro-elastic media. J. Math. Anal. Appl. **251**, 310–340 (2000)
43. Wang, J., Mathew, T.P.: Mixed finite element method over quadrilaterals. In: Dimov, I.T., Sendov, B., Vassilevski, P. (eds.): Conference on Advances in Numerical Methods and Applications, pp. 203–214. World Scientific, River Edge (1994)
44. Wheeler, M.F., Yotov, I.: A multipoint flux mixed finite element method. SIAM J. Numer. Anal. **44**, 2082–2106 (2006)
45. Wheeler, M., Xue, G., Yotov, I.: Benchmark 3D: a multipoint flux mixed finite element method on general hexahedra. In: Finite Volumes for Complex Applications VI Problems & Perspectives. Springer Proceedings in Mathematics, vol. 4, pp. 1055–1065 (2011)
46. Wheeler, M., Xue, G., Yotov, I.: Accurate cell-centered discretizations for modeling multiphase flow in porous media on general hexahedral and simplicial grids. SPE J. **7**, 779–793 (2012)
47. Wheeler, M., Xue, G., Yotov, I.: A multipoint flux mixed finite element method on distorted quadrilaterals and hexahedra. Numer. Math. **121**, 165–204 (2012)